Cerebellum instructs plasticity in the mouse primary somatosensory cortex

Authors: Abby Silbaugh[1], Kevin P. Koster[1], Christian Hansel[1]*

Affiliation:

[1]Department of Neurobiology and Neuroscience Institute, University of Chicago; Chicago, 60637, USA.

*Corresponding author. Email: chansel@bsd.uchicago.edu.

Abstract: Sensory experiences map onto distributed neural networks and may activate plasticity processes that in some brain areas are supervised by instructive signals. What remains unknown, however, is if such instructive signals influence plasticity beyond local circuits. Here, we show that optogenetic activation of climbing fibers, which provide instructive signals in cerebellar plasticity, suppresses whisker response potentiation in L2/3 pyramidal cells of the primary somatosensory cortex of mice. Using two-photon imaging and chemogenetics, we find that plasticity is controlled by modulating activity levels of VIP- and SST- positive interneurons. Transsynaptic labeling identifies zona incerta to thalamic posterior medial nucleus projections as the main pathway for cerebellar output reaching cortex. Our findings show that neocortical plasticity is not self-organized but depends on supervision by the olivo-cerebellar system.

Main Text:

Learning in the cerebral cortex is assumed to be predominantly driven by the input signal itself, classifying it as unsupervised (*1*). For example, plasticity in the barrel field of the primary somatosensory cortex (S1 cortex) of rodents is evoked upon repeated whisker stimulation. This plasticity may reorganize receptive field maps after whisker clipping (*2-4*) or reflect a history of rhythmic whisker stimulation (*5-7*) that necessitates adaptive plasticity of synaptic weights, e.g. via long-term potentiation (LTP) and/or long-term depression (LTD) at synaptic inputs onto pyramidal neurons (*8, 9*). The high degree of plasticity in S1 somatosensory circuits enables adaptation to altered input structures (*10*).

Supervised learning, in contrast, is typical for the cerebellum (*1*). Depending on dendritic architecture, Purkinje cells (PCs) receive input from one or more climbing fibers (CFs; *11*) that originate in the contralateral inferior olive (IO). As originally predicted by Marr in his *Theory of Cerebellar Cortex*, climbing fiber signaling supervises plasticity at cerebellar parallel fiber (PF) – PC synapses, providing *contexts* for motor learning (*12*). Marr's prediction of PF-LTP resulting from CF co-activation was later corrected by Albus, who instead proposed LTD to more appropriately drive motor circuit activation (*13*) as PCs themselves provide inhibitory input to their target neurons in the cerebellar nuclei (*14*). It was later experimentally verified that PF and CF co-stimulation initiates LTD at PF synapses (*15, 16*), and that the CF – via evoked calcium transients – tightly controls plasticity at these synapses (*17-22*) and provides essential instructive signals for cerebellum-controlled motor learning (*23-26*).

The cerebellum projects via the thalamus to motor cortex and non-motor areas, including the prefrontal cortex (*27-28*), sensory and associative areas (29-31). A plausible possibility is therefore that cerebellar output impacts cortical signaling. It has indeed been shown that the cerebellum modulates the coherence of neuronal oscillations between neocortical areas (*32-34*), suggestive of a role even in cognitive and social functions (*35, 36*). Here, we specifically asked whether CFs can provide instructive signals outside of their exclusive projection areas in the cerebellum. Our observation that CF signaling supervises adaptive plasticity in S1 cortex indeed demonstrates that instructive signaling can involve anatomically segregated brain regions.

Activity-dependent plasticity in S1 cortex is suppressed by optogenetic CF activation

To study the effects of optogenetic CF co-activation on S1 plasticity, we expressed GCaMP6f in neurons in S1 cortex and used two-photon microscopy in awake mice to measure responses to air puff stimulation of the whisker field in neurons in superficial layers 2 and 3 (Fig. 1A+D). For optogenetic CF activation, channelrhodopsin-2 (ChR2) was expressed in neurons of the inferior olive (IO), which give rise to CFs terminating in the contralateral cerebellar cortex (Fig. 1B+E). The efficacy of optogenetic activation was tested by expressing GCaMP6f in PCs of crus I/II and measuring calcium transients evoked by 470nm, 50ms LED light pulses (Fig. 1C; Fig. S1). For plasticity induction in S1 cortex, we used a multi-whisker stimulation protocol ('rhythmic whisker stimulation'; RWS) that consisted of an application of 100ms air puffs (8psi) to the contralateral whisker field (*37, 38*) for 5min at 8Hz, which is a natural whisking frequency for mice that are sampling the environment (*39*). RWS stimulation resulted in an increase in whisker-evoked calcium responses ($\Delta F/F$ over the range of 0-700ms post-stimulus onset) that we observed in morphologically identified L2/3 pyramidal neurons (PNs; Fig. 1F) for the duration of the recording (60min post-RWS; Fig. 1G-I). These somatic calcium response amplitudes correlate with neuronal spike rates (*40*). L2/3 pyramidal neurons respond to stimulation of the

corresponding principal whisker but may also respond to stimulation of surround whiskers (*41*). Therefore, the plasticity observed here in response to multi-whisker stimulation may reflect both a potentiation of synapses conveying already existing whisker input as well as an expansion of the neuron's receptive field to include additional surround whiskers. When CFs in crus I/II of the cerebellum were optogenetically co-activated with 470nm, 50ms LED light pulses at 1Hz for 5min during the period of repeated stimulation (RWS+CF), the potentiation of L2/3 pyramidal cell responses in S1 cortex was absent and depression was observed instead (Fig. 1G-I; Fig. S2). Neurons that were not identified as pyramidal cells (i.e. putative interneurons; INs) collectively responded to RWS stimulation with a significant depression in the amplitude of evoked calcium events, which was absent upon optogenetic CF co-activation (Fig. 1J-L; Fig. S2). Both the S1 plasticity and optogenetic CF activation effects were observed when trials with active movement of the mouse were included (Fig. 1; Fig. S2) or when analysis was restricted to trials during which the mice were resting both before and after stimulus onset (Fig. S3).

We reproduced these findings using an alternate methodology that is well suited to detect receptive fields, including barrels in S1 cortex. Intrinsic optical imaging (*42*) was used to measure plasticity effects at low spatial resolution in anesthetized mice to facilitate measurement of single whisker responses. We slipped a glass pipette over an individual untrimmed whisker and moved it back and forth at 10Hz for a period of 5min. In the barrel field of contralateral S1 cortex, we confirmed the activation of the corresponding barrel and recorded responses to this passive sensory experience for 20min before and 30min after repeated stimulation. We observed an increase in the responsive area beyond the barrel (Fig. S4) that was not seen in the absence of repeated stimulation (Fig. S4). When ChR2-expressing CFs in crus I/II of the cerebellum were optogenetically activated at 1Hz for 5min during the period of repeated stimulation, this plasticity was not observed in S1 cortex (Fig. S4). Thus, intrinsic optical imaging demonstrates receptive field plasticity of barrels is regulated by cerebellar instructive signaling.

Our findings from two-photon imaging demonstrate that whisker-induced response potentiation in S1 cortex results from L2/3 pyramidal cell plasticity. Interneurons show the opposite direction of plasticity (and same sensitivity to CF co-activation), suggesting a critical role of the inhibitory network in S1 cortex. The non-corresponding temporal profile of RWS-evoked plasticity in pyramidal cells and interneurons (Fig. 1H+K), however, demonstrates that pyramidal cell-LTP is not exclusively caused by interneuron-LTD, although some contribution seems possible.

CF activation modulates inhibitory interneurons in S1 cortex

To further identify the origin of the suppressive effect of optogenetic CF activation on S1 plasticity, we next determined how the basic whisker response properties of specific neuron types in the S1 circuit are altered during CF co-activation (Fig. 2A). To begin with, we observed that these basic responses are not significantly changed in the population of examined L2/3 pyramidal neurons upon optogenetic CF activation (Fig. 2B; 0-700ms analysis window). However, we found that in 11/23 mice, an overall response decrease resulted from CF co-activation, while in 5/23 mice an increase was seen (10% threshold). Significance in the observed mild response reduction emerged in the analysis across all neurons when a late analysis window was selected (650-850ms). These findings suggest that CF co-activation causes a range of response changes in the population of L2/3 pyramidal neurons, but that an overall suppressive effect becomes apparent in the late response phase.

In the same mice, the basic responses of putative interneurons to whisker stimulation were increased upon CF co-activation (Fig. 2C). Given parvalbumin (PV)-positive interneurons, somatostatin (SST)-positive interneurons, and vasoactive intestinal polypeptide (VIP)-positive interneurons make up ~40%, ~30%, and ~12% of the neocortical interneuron population (*43, 44*), respectively, these basic response increases – and the plasticity measures from the population of non-pyramidal cells (Fig. 1J-L) – are likely comprised of a substantial proportion of PV and SST interneurons. Using tdTomato-tagged interneurons to record from these distinct interneuron subpopulations in a similar series of two-photon recordings (Fig. 2D-F), we showed that basic responses to whisker stimulation were indeed enhanced in SST and PV interneurons upon CF co-activation (Fig. 2G-I). VIP interneurons, which primarily inhibit other interneurons including SST and PV interneurons, showed no consistent change in their basic responses to whisker stimulation upon CF co-activation in the default analysis window (0-700ms; Fig. 2G). However, like pyramidal neurons (Fig. 2B), VIP interneurons demonstrated significant suppression in the late analysis window of 650-850ms (Fig. 2G). We used the same mice to examine RWS- and RWS+CF-induced plasticity effects in groups of tdTomato-tagged interneurons that directly inhibit L2/3 pyramidal neurons. In this interneuron population, RWS stimulation caused a significant depression that was absent following RWS+CF (Fig. S2), consistent with our observations in putative interneurons (Fig. 1J-L).

Opposing roles of SST and VIP interneurons in CF-mediated control of S1 plasticity

As SST interneurons are activated by CF co-activation, we tested whether they assume a key role in the CF-mediated suppression of S1 plasticity. To do so, we next used chemogenetic approaches for activity manipulation. We focused on SST rather than PV interneurons, because SST interneurons contact the dendrites of L2/3 pyramidal cells (Fig. 3A+E), where inhibition can impact local synaptic plasticity processes. This selection does not exclude a potential role for PV interneurons. However, these cells are usually basket cells with control over action potential generation rather than dendritic signal integration and are therefore less well positioned to modulate synaptic plasticity. We expressed the excitatory hM3D(Gq) DREADDs in SST interneurons (Fig. 3B). Administration of the DREADD agonist deschloroclozapine (DCZ) by intraperitoneal injection caused an increase in SST interneuron responses (Fig. 3C; Fig. S5). Under these conditions, RWS did not potentiate L2/3 pyramidal cell responses and calcium signals were depressed instead, mimicking the results of optogenetic CF co-activation (Fig. 3D; Fig. S5). In contrast, inhibitory hM4D(Gi) DREADD expression in SST interneurons (Fig. 3F) and acute administration of DCZ caused a significant reduction in SST interneuron responses (Fig. 3G; Fig. S5). This rescued potentiation of L2/3 pyramidal cell responses when RWS was paired with CF co-activation (Fig. 3H; Fig. S5). These findings confirm that SST interneurons are in a position to control plasticity of L2/3 pyramidal neurons (*9*) and suggest that this mechanism is recruited by CF co-activation.

VIP interneurons inhibit SST interneurons (Fig. 4A+E) and may suppress SST interneuron activity during RWS, thus enabling plasticity (*9, 45*). We have shown above that optogenetic CF activation reduces whisker-evoked responses in a subset of VIP interneurons (Fig. 2). To examine whether this activity regulation is critical for RWS+CF-induced suppression of L2/3 pyramidal cell plasticity, we used chemogenetic approaches to manipulate the activity of VIP interneurons. We indeed observed that expression of inhibitory hM4D (Gi) DREADDs in VIP interneurons (Fig. 4B) and acute DCZ administration significantly reduced activity in VIP interneurons (Fig. 4C; Fig. S5) and prevented S1 potentiation upon RWS

stimulation alone (Fig. 4D; Fig. S5) – similar to the effect of SST or CF activation during RWS. Conversely, expression of excitatory hM3D(Gq) DREADDs in VIP interneurons (Fig. 4F) and acute DCZ administration enhanced VIP interneuron responses (Fig. 4G; Fig. S5) and rescued S1 plasticity upon paired RWS and optogenetic CF activation (RWS+CF; Fig. 4H; Fig. S5), mimicking the effect of suppressing SST interneuron activity during RWS+CF. These findings confirm that VIP interneurons orchestrate the inhibitory network in S1 cortex and show that this mechanism is recruited by optogenetic CF activation. Together with the results demonstrating S1 interneuron responses to basic whisker stimulation are differentially modulated by CF co-activation (Fig. 2), these observations also show that the critical circuit for S1 plasticity and its regulation is located – at least partially – in S1 cortex itself. Modulation provided by instructive signals is therefore triggered within S1 cortex and does not need to be delivered from outside it.

Zona incerta to the thalamic posterior medial nucleus (POm) as a multi-synaptic pathway from the cerebellar nuclei to S1 cortex

The barrel cortex in mice receives whisker sensory information from two thalamic sources, the ventral posterior medial thalamic nucleus (VPM), and the posterior medial thalamic nucleus (POm). Whereas the VPm projects densely to the middle layers of S1 cortex, POm inputs terminate largely in L5 as well as L1, where, in addition to pyramidal cells, they synapse on VIP interneurons (*46, 47*). However, the cerebellar nuclei do not directly project to either VPm or POm. Therefore, we investigated a potential pathway from the cerebellar nuclei to the superficial layers of S1 cortex through the zona incerta (ZI), a subthalamic area that receives input from all three cerebellar nuclei (*48*) and projects to POm (*49*). To this end, we first determined primary output pathways of ZI cells that receive cerebellar input by leveraging the transsynaptic transport properties of AAV1 (*50*). AAV1-Flp recombinase (pAAV-EF1a-Flpo) was delivered to the deep cerebellar nuclei, followed by a Flp-dependent label (Frt-ChR2-EYFP) to contralateral ZI. Abundant EYFP-expressing neurons were found in the ZI (Fig. 5A+B; Fig. S6), with their labeled axons projecting to both POm (Fig. 5A+B; Fig. S6) and S1 cortex (Fig. 5A+B). In separate experiments, we used retrograde fluorogold labeling from the somatosensory thalamus to mark the thalamic reticular nucleus (TRN), whose GABAergic neurons inhibit VPM. We found no overlap with transsynaptic labeling from the contralateral cerebellar nuclei in TRN (Fig. S7), which suggests that the ZI-POm pathway, and not the TRN-VPM pathway, constitutes the main thalamic route for cerebellar signals reaching S1 cortex (Fig. S7).

To assess whether there is a monosynaptic connection from the cerebellar nuclei to neurons in the ZI that project to POm, we induced ChR2 expression in the cerebellar nuclei and performed *in vitro* whole-cell patch-clamp recordings from POm-projecting ZI neurons (i.e. cells that were retrogradely labeled by fluororuby injected into POm) and tested them for ChR2-evoked responses (Fig. 5D). Optogenetic activation of ChR2+ terminals at 10Hz elicited EPSPs that persisted in the presence of bath-applied TTX (1 μM; Fig. 5E+F), despite significant amplitude reduction. This TTX-insensitive component represents the ChR2-evoked EPSP at the synapses between cerebellar nuclei neurons and ZI neurons and demonstrates the monosynaptic nature of this pathway (*51*).

It has previously been demonstrated that most POm-projecting neurons in ZI are PV interneurons (*52*). To test whether these neurons convey cerebellar instructive signals to S1 cortex, we chemogenetically inhibited PV interneurons in ZI during basic whisker and whisker plus optogenetic CF activation conditions and measured responses in L2/3 pyramidal neurons in

S1 cortex. Expression of inhibitory hM4D (Gi) DREADDs in ZI-residing PV interneurons (Fig. 5G) and DCZ application prevented the suppressive effect of CF co-activation on pyramidal cell responses (Fig. 5H+I). These data identify thalamically projecting PV interneurons in ZI as the conveyor of instructive CF signals from the cerebellum to the neocortex.

Discussion

Multiple functions have been assigned to cerebellar CFs. They provide instructive error signals (*53*), convey sensory input across modalities (e.g. *54-58*), and may even signal the absence of expected sensory signals (*59*). CFs may also carry reward or reward prediction-related signals (*60, 61*). As in our recordings CF co-activation suppresses S1 plasticity in an experimental paradigm lacking behavioral reward, we interpret the CF input as conveying an error signal. However, it remains possible that CF recruitment and suppression of S1 plasticity may happen in a reward / reward omission context as well. CF activation might be driven by reward / reward omission in sensory-association training. This might be the reason why sensory stimulation in such training context drives cortical plasticity less well than passive sensory stimulation alone (*62*). Plasticity in S1 cortex results from an update in sensory input – here exposure to a new passive sensory experience – that necessitates circuit adaptation. CF signaling may get recruited when an obvious disruption or violation of a sensory prediction occurs, or simply when no stability in sensory input is reached. The absence of *sameness* may be detected by inferior olive neurons as an error in the sensory environment, and subsequently CFs enforce an interruption of adaptive plasticity.

In rodents, direct trigemino-olivary connections convey whisker-related information to the olive (*63*). Passive whisker activation evokes CF-mediated complex spike firing in PCs (*54*). These evoked spikes occur on top of a spontaneous complex spike firing rate of ~1Hz (*53*). What distinguishes CF activity that suppresses plasticity in the cerebral cortex from these more common activity patterns? First, prolonged low-frequency air puff stimulation to sensitive skin areas on the snout or wrist of rodents evokes potentiation, and not depression, of PC responses (*64, 65*). This finding indicates that when stimuli are repeatedly presented (producing/inhabiting a state of *sameness*), complex spike firing ceases. Second, the synchronization of CF responses might be critical. Complex spike synchrony is absent or weak during spontaneous activity and might increase with movement initiation (*66, 67*) or sensory stimulation (*68*). Synchrony in a sufficiently high number of PCs is needed to evoke inhibition and subsequent rebound excitation in target neurons in the cerebellar nuclei (*69, 70*). Parallel fibers (PFs) likely cannot generate synchronous activity in enough PCs due to the spatial arrangement of PF input (*71*). A threshold level of synchronization will be reached with optogenetic CF activation, but may also naturally be reached with specific qualities of the sensory input signal, e.g. those that make it an error signal. It is also conceivable that synchronization to a threshold level is driven by an error signal that does not originate from whisker stimulation but has another sensory or non-sensory origin.

Whisker-related sensory information in rodents is conveyed by the trigeminal ganglion via thalamic nuclei VPM and POm to the barrel cortex; information from specific whiskers is projected via VPM to cortical layer 4 (*72*). The observation that cerebellar instructive signals impact S1 cortex via ZI and POm fits the description of a more modulatory pathway that does not interfere with thalamic input in layer 4, but with synaptic signal integration in the more superficial as well as deeper layers. Both two-photon imaging and chemogenetics identify SST interneurons in S1 cortex as the ultimate mediators of the activation of this modulatory pathway.

These, in turn, are regulated by VIP interneurons that receive activation from POm (*46*). We identified PV interneurons in ZI as neurons that are critically involved in this pathway as well, likely reducing the POm-mediated activation of VIP interneurons in S1 cortex. These are all well-described circuit elements in thalamo-cortical communication. Our findings demonstrate that cerebellar output may recruit PV interneurons in ZI sufficiently well to ultimately cause a removal of VIP interneuron-mediated inhibition of SST interneurons and consequently enhance dendritic inhibition of L2/3 pyramidal neurons. Another context where PV interneurons in the ZI become activated – via glutamatergic input from S1 cortex – is self-grooming in the orofacial area (*73*). It is plausible that under such conditions of predicted sensory input, whisker-related L2/3 pyramidal neuron plasticity is suppressed as well.

Our data show that plasticity in S1 cortex of the mouse does not solely depend on activity within S1 circuits, but it additionally depends on an explicit feedback signal provided by a non-cortical brain area. Therefore, this plasticity is not exclusively self-organized, but it is additionally supervised (*74*). This observation is in contradiction to the notion that learning in the cerebral cortex is solely directed by the input signal itself and therefore unsupervised, while supervised learning is characteristic for the cerebellum (*1*). The observed external supervision enables regulatory control that might safeguard the cerebral cortex from maladaptation, albeit at the cost of exposing it to pathological dysfunction of the olivo-cerebellar system, e.g. sensory over-responsivity that has been described in syndromic autism (*75*).

References and Notes

1. K. Doya, Complementary roles of basal ganglia and cerebellum in learning and motor control. *Curr. Opin. Neurobiol*. **10**, 732-739 (2000).
2. M. E. Diamond, M. Armstrong-James, F. F. Ebner, Experience-dependent plasticity in adult rat barrel cortex. *Proc. Natl. Acad. Sci. USA* **90**, 2082-2086 (1993). Doi:10.1073/pnas.905.2082.
3. S. Glazewski, A. L. Barth, H. Wallace, M. McKenna, A. Silva, K. Fox, Impaired experience-dependent plasticity in barrel cortex of mice lacking the alpha and delta isoforms of CREB. Cereb. Cortex **9**, 249-256 (1999).
4. E.A. Stern, M. Maravall, K. Svoboda, Rapid development and plasticity of layer 2/3 maps in rat barrel cortex in vivo. *Neuron* **31**, 305-315 (2001). Doi: 10.1016/s0896-6273(01)00360-9.
5. J. Delacour, O. Houcine, J. C. Costa, Modifications of the responses of barrel field neurons to vibrissal stimulation during theta in the awake and undrugged rat. *Neuroscience* **37**, 237-243 (1990).
6. P. Megevand, E. Troncoso, C. Quairiaux, D. Muller, C. M. Michel, J. Z. Kiss, Long-term plasticity in mouse sensorimotor circuits after rhythmic whisker stimulation. *J. Neurosci*. **29**, 5326-5335 (2009).
7. F. Gambino, S. Pages, V. Kehayas, D. Baptista, R. Tatti, A. Carleton, A. Holtmaat, Sensory-evoked LTP driven by dendritic plateau potentials in vivo. *Nature* **515**, 116-119 (2014).
8. D. E. Feldman, Timing-based LTP and LTD at vertical inputs to layer II/III pyramidal cells in rat barrel cortex. *Neuron* **27**, 45-56 (2000).
9. L. E. Williams, A. Holtmaat, Higher-order thalamocortical inputs gate synaptic long-term potentiation via disinhibition. *Neuron* **101**, 91-102 (2019).

10. D. E. Feldman, M. Brecht, Map plasticity in somatosensory cortex. *Science* **310**, 810-815 (2005).

11. S. E. Busch, C. Hansel, Climbing fiber multi-innervation of mouse Purkinje dendrites with arborization common to human. *Science* **381**, 420-427 (2023).

12. D. Marr, A theory of cerebellar cortex. *J. Physiol*. **202**, 437-470 (1969).

13. J. S. Albus, A theory of cerebellar function. *Math. Biosci*. **10**, 25-61 (1971).

14. M. Ito, M. Yoshida. The cerebellar-evoked monosynaptic inhibition of Deiters' neurons. *Experientia* **20**, 515-516 (1964).

15. M. Ito, M. Kano, Long-lasting depression of parallel fiber-Purkinje cell transmission induced by conjunctive activation of parallel fibers and climbing fibers in the cerebellar cortex. *Neurosci. Lett*. **33**, 253-258 (1982).

16. M. Ito, M. Sakurai, P. Tongroach, Climbing fibre induced depression of both mossy fibre responsiveness and glutamate sensitivity of cerebellar Purkinje cells. *J. Physiol*. **265**, 833-854 (1982).

17. S. S. Wang, W. Denk, M. Häusser, Coincidence detection in single dendritic spines mediated by calcium release. *Nat. Neurosci*. **3**, 1266-1273 (2000).

18. V. Lev-Ram, S. T. Wong, D. R. Storm, R. Y. Tsien, A new form of cerebellar potentiation is postsynaptic and depends on nitric oxide but not cAMP. *Proc. Natl. Acad. Sci. USA* **99**, 8389-8393 (2002).

19. M. Coesmans, J. T. Weber, C. I. De Zeeuw, C. Hansel, Bidirectional parallel fiber plasticity in the cerebellum under climbing fiber control. *Neuron* **44**, 691-700 (2004).

20. C. Piochon, H. K. Titley, D. H. Simmons, G. Grasselli, Y. Elgersma, C. Hansel, Calcium threshold shift enables frequency-independent control of plasticity by an instructive signal. *Proc. Natl. Acad. Sci. USA* **113**, 13221-13226 (2016).

21. A. Suvrathan, H. L. Payne, J. L. Raymond, Timing rules for synaptic plasticity matched to behavioral function. *Neuron* **92**, 959-967 (2016).

22. H. K. Titley, M. Kislin, D. H. Simmons, S. S. Wang, C. Hansel, Complex spike clusters and false-positive rejection in a cerebellar supervised learning rule. *J. Physiol*. **597.16**, 4387-4406 (2019).

23. J. F. Medina, J. C. Repa, M. D. Mauk, J. E. LeDoux, Parallels between cerebellum- and amygdala-dependent conditioning. *Nat. Rev. Neurosci*. **3**, 122-131 (2002).

24. Y. Yang, S. G. Lisberger, Interaction of plasticity and circuit organization during the acquisition of cerebellum-dependent motor learning. *eLife* **2**, e01574 (2013).

25. Y. Yang, S. G. Lisberger, Purkinje-cell plasticity and cerebellar motor learning are graded by complex-spike duration. *Nature* **510**, 529-532 (2014).

26. N. T. Silva, J. Ramirez-Buritica, D. L. Pritchett, M. R. Carey, Climbing fibers provide essential instructive signals for associative learning. *Nat. Neurosci*. **27**, 940-951 (2024).

27. F. A. Middleton and P. L. Strick, Cerebellar projections to the prefrontal cortex of the primate. *J. Neurosci*. **21**, 700-712 (2001).

28. P. L. Strick, R. P. Dum, J. A. Fiez, Cerebellum and non-motor function. *Annu. Rev. Neurosci*., **32**, 413-434 (2009).

29. A. Badura, J. L. Verpeut, J. W. Metzger, T. D. Pereira, T. J. Pisano, B. Deverett, D. E. Bakshinskaya, S. S. Wang, Normal cognitive and social development require posterior cerebellar activity. *eLife* **7**, e36401 (2018).

30. E. Kelly et al., Regulation of autism-relevant behaviors by cerebellar-prefrontal cortical circuits. *Nat. Neurosci*. **23**, 1102-1110 (2020).

31. T. J. Pisano et al., Homologous organization of cerebellar pathways to sensory, motor, and associative forebrain. *Cell Rep*. **36**, 109721 (2021).

32. D. Popa, M. Spolidoro, R. D. Proville, N. Guyon, L. Belliveau, C. Lena, Functional role of the cerebellum in gamma-band synchronization of the sensory and motor cortices. *J. Neurosci*. **33**, 6552-6556 (2013).

33. S. McAfee, Y. Liu, R. V. Sillitoe, D. H. Heck, Cerebellar lobulus simplex and Crus I differentially represent phase and phase difference of prefrontal cortical and hippocampal oscillations. *Cell Rep*. **27**, 2328-2334 (2019).

34. S. Lindeman, S. Hong, L. Kros, J. F. Mejias, V. Romano, R. Oostenveld, M. Negrello, L. W. Bosman, C. I. De Zeeuw, Cerebellar Purkinje cells can differentially modulate coherence between sensory and motor cortex depending on region and behavior. *Proc. Natl. Acad. Sci. USA* **118**, e2015292118 (2021).

35. J. D. Schmahmann, J. C. Sherman, The cerebellar cognitive affective syndrome. *Brain* **121**, 561-579 (1998).

36. C. J. Stoodley, P. T. Tsai, Adaptive prediction for social contexts: the cerebellar contribution to typical and atypical social behaviors. *Annu. Rev. Neurosci*. **44**, 475-493 (2021).

37. J. S. Jouhanneau, L. Ferrarese, L. Estebanez, N. J. Audette, M. Brecht, A. L. Barth, J. F. Poulet, Cortical fosGFP expression reveals broad receptive field excitatory neurons targeted by Pom. *Neuron* **84**, 1065-1078 (2014).

38. N. J. Audette, S. M. Bernhard, A. Ray, L. T. Stewart, A. L. Barth, Rapid plasticity of higher-order thalamocortical inputs during sensory learning. *Neuron* **103**. 277-291 (2019).

39. M. E. Diamond, M. von Heimendahl, P. M. Knutsen, D. Kleinfeld, E. Ahissar, 'Where' and 'what' in the whisker sensorimotor system. *Nature Rev. Neurosci*. **9**, 601-612 (2008).

40. Y. Zhang et al., Fast and sensitive GCaMP calcium indicators for imaging neural populations. *Nature* **615**, 884-891 (2023).

41. M. Brecht, A. Roth, B. Sakmann, Dynamic receptive fields of reconstructed pyramidal cells in layers 2 and 3 of rat somatosensory barrel cortex. *J. Physiol*. **553**, 243-265 (2003).

42. T. Bonhoeffer, A. Grinvald, Iso-orientation domains in cat visual cortex are arranged in pinwheel-like patterns. *Nature* **353**, 429-431 (1991).

43. J.F. Staiger, C.C.H. Petersen, Neuronal circuits in barrel cortex for whisker sensory perception. *Physiol. Rev*. **101**, 353-415 (2021).

44. R. Tremblay, S. Lee, B. Rudy, GABAergic interneurons in the neocortex: from cellular properties to circuits. *Neuron* **91**, 260-292 (2016).

45. L. E. Williams, L. Küffer, T. Bawa, E. Husi, S. Pagès, A. Holtmaat, Repetitive sensory stimulation potentiates and recruits sensory-evoked cortical population activity. *J. Neurosci*. **45**, e2189232024 (2025).

46. N. J. Audette, J. Urban-Cieko, M. Matsushita, A. L. Barth, POm thalamocortical input drives layer-specific microcircuits in somatosensory cortex. *Cereb. Cortex* **28**, 1312-1328 (2018).

47. B. S. Sermet, P. Truschow, M. Feyerabend, J. M. Mayrhofer, T. B. Oram, O. Yizhar, J. F. Staiger, C. C. H. Petersen, Pathway- layer- and cell-type-specific thalamic input to mouse barrel cortex. *eLife* **8**, e52665 (2019).

48. M. Novello, L.W. Bosman, C. I. De Zeeuw, A systematic review of direct outputs from the cerebellum to the brainstem and diencephalon in mammals. *Cerebellum* **23**, 210-239 (2022).

49. P. Bartho, T. F. Freund, L. Acsady, Selective GABAergic innervation of thalamic nuclei from zona incerta. *Eur. J. Neurosci*. **16**, 999-1014 (2002).

50. B. Zingg, X.L. Chou, Z.G. Zhang, L. Mesik, F. Liang, H.W. Tao, L.I. Zhang, AAV-mediated anterograde transsynaptic tagging: mapping corticocollicular input-defined neural pathways for defense behaviors. *Neuron* **93**, 33-47 (2017).

51. J.H. Cho, K. Deisseroth, V.Y. Bolshakov, Synaptic encoding of fear extinction in mPFC-amygdala circuits. *Neuron* **80**, 1491-1507 (2013).

52. J. C. Trageser, K. A. Burke, R. Masri, Y. Li, L. Sellers, A. Keller, State-dependent gating of sensory inputs by zona incerta. *J. Neurophysiol*. **96**, 1456-1463 (2006).

53. J. I. Simpson, D. R. Wylie, C. I. De Zeeuw, On climbing fiber signals and their consequence(s). *Behav. Brain Sci*. **19**, 384-398 (1996).

54. L. W. Bosman, S. K. Koekkoek, J. Shapiro, B. F. Rijken, F. Zandstra, B. van der Ende, C. B. Owens, J. W. Potters, J. R. de Gruijl, T. J. Ruigrok, C. I. De Zeeuw, Encoding of whisker input by cerebellar Purkinje cells. *J. Physiol*. **588**, 3757-3783 (2010).

55. D. J. Herzfeld, R. Shadmehr, Cerebellum estimates the sensory state of the body. *Trends Cogn. Neurosci*. **18**, 66-67 (2014).

56. F. Najafi, A. Giovannucci, S. S. Wang, J. F. Medina, Sensory-driven enhancement of calcium signals in individual Purkinje dendrites of awake mice. *Cell Rep*. **6**, 792-798 (2014a).

57. F. Najafi, A. Giovannucci, S. S. Wang, J. F. Medina, Coding of stimulus strength via analog calcium signals in Purkinje cell dendrites of awake mice. *eLife* **3**, e03663 (2014b).

58. M. A. Gaffield, A. Bonnan, J. M. Christie, Conversion of graded presynaptic climbing fiber activity into graded postsynaptic Ca2+ signals by Purkinje cell dendrites. *Neuron* **102**, 762-769 (2019).

59. S. Ohmae, J. F. Medina, Climbing fibers encode a temporal-difference prediction error during cerebellar learning in mice. *Nat. Neurosci*. **18**, 1798-1803 (2015).

60. W. Heffley, C. Hull, Classical conditioning drives learned reward prediction signals in climbing fibers across the lateral cerebellum. *eLife* **8**, e46764 (2019).

61. D. Kostadinov, M. Beau, M. Blano-Pozo, M. Häusser, Predictive and reactive reward signals conveyed by climbing fiber inputs to cerebellar Purkinje cells. *Nat. Neurosci*. **22**, 950-962 (2019).

62. M. Zhu, S. J. Kuhlman, A. L. Barth, Transient enhancement of stimulus-evoked activity in neocortex during sensory learning. *Learn. Mem*. **31**, a053870.123 (2024).

63. L.W. Bosman, A.R. Houweling, C.B. Owens, N. Tanke, O.T. Shevchouk, N. Rahmati, W.H. Teunissen, C. Ju, W. Gong, S.K. Koekkoek, C.I. De Zeeuw, Anatomical pathways involved in generating and sensing rhythmic whisker movements. *Front. Integr. Neurosci*. **5**, 53 (2011).

64. K.B. Ramakrishnan, K. Voges, L. De Propris, C.I. De Zeeuw, E. D'Angelo, Tactile stimulation evokes long-lasting potentiation of Purkinje cell discharge in vivo. *Front. Cell. Neurosci*. **10**, 36 (2016).

65. T.F. Lin, S.E. Busch, C. Hansel, Intrinsic and synaptic determinants of receptive field plasticity in Purkinje cells of the mouse cerebellum. *Nat. Commun*. **15**, 4645 (2024).

66. J. P. Welsh, Functional significance of climbing-fiber synchrony. A population coding and behavioral analysis. *Ann. N. Y. Acad. Sci*. **978**, 188-204 (2002).

67. S. Kitazawa, D. M. Wolpert, Rhythmicity, randomness and synchrony in climbing fiber signals. *Trends Neurosci*. **28**, 611-619 (2005).

68. S. R. Schultz, K. Kitamura, A. Post-Uiterweer, J. Krupic, M. Häusser, Spatial pattern coding of sensory information by climbing fiber-evoked calcium signals in networks of neighboring cerebellar Purkinje cells. *J. Neurosci*. **29**, 8005-8015 (2009).

69. V. Gauck, D. Jaeger, The control of rate and timing of spikes in the deep cerebellar nuclei by inhibition. *J. Neurosci*. **20**, 3006-3016 (2000).

70. A. L. Person, I. M. Raman, Purkinje neuron synchrony elicits time-locked spiking in the cerebellar nuclei. *Nature* **481**, 502-506 (2012).

71. T. Tang, T.A. Blenkinsop, E.J. Lang, Complex spike synchrony dependent modulation of rat deep cerebellar nuclear activity. *eLife* **8**, e40101 (2019).

72. D. Feldmeyer, M. Brecht, F. Helmchen, C.C.H. Petersen, J. F. Poulet, J. F. Staiger, H. J. Luhmann, C. Schwarz, Barrel cortex formation. *Prog. Neurobiol*. **103**, 3-27 (2013).

73. J. Ge, P. Ren, B. Tian, J. Li, C. Qi, Q. Huang, K. Ren, E. Hu, H. Mao, Y. Zang, S. Wu, Q. Xue, W. Wang, Ventral zona incerta parvalbumin neurons modulate sensory-induced and stress-induced self-grooming via input-dependent mechanisms in mice. *iScience* **27**, 110165 (2024).

74. E. I. Knudsen, Supervised learning in the brain. *J. Neurosci*. **14**, 3985-3997 (1994).

75. D. H. Simmons, S. E. Busch, H. K. Titley, G. Grasselli, J. Shi, X. Du, C. Wei, C. M. Gomez, C. Piochon, C. Hansel, Sensory over-responsivity and aberrant plasticity in cerebellar cortex in a mouse model of syndromic autism. *Biol. Psychiatry: GOS* **2**, 450-459 (2022).

76. C. Viollet, A. Simon, V. Tolle, A. Labarthe, D. Grouselle, Y. Loe-Mie, M. Simonneau, G. Martel, J. Epelbaum. Somatostatin-IRES-Cre Mice: Between Knockout and Wild-Type? *Front Endocrinol* **8** (2017).

77. A. H. Cheng, S. W. Fung, H. M. Cheng. Limitations of the Avp-IRES2-Cre (JAX #023530) and Vip-IRES-Cre (JAX #010908) Models for Chronobiological Investigations. *J Biol Rhythms* **34**, 634-644 (2019).

78. K. P. Koster, S. M. Sherman. Convergence of inputs from the basal ganglia with layer 5 of motor cortex and cerebellum in mouse motor thalamus. *eLife* **13**, e97489 (2024).

79. G. Paxinos, K. B. J. Franklin. *Paxinos and Franklin's The Mouse Brain in Stereotaxic Coordinates* (Elsevier, ed. 5, 2019).

80. T. Miyazaki, M. Watanabe. Development of an anatomical technique for visualizing the mode of climbing fiber innervation in Purkinje cells and its application to mutant mice lacking GluRδ2 and Ca(v)2.1. *Anat Sci Int* **86 (**2011).

81. B. Vasquez, B. Campos, A. Cao, A. T. Theint, W. Zeiger. High-Sensitivity Intrinsic Optical Signal Imaging Through Flexible, Low-Cost Adaptations of an Upright Microscope. *eNeuro* **10** (2023).

82. A. Ayaz, A. Stäuble, M. Hamada, M. A. Wulf, A. B. Saleem, F. Helmchen. Layer-specific integration of locomotion and sensory information in mouse barrel cortex. *Nature Commun* **10**, 2585 (2019).

Acknowledgments:

We thank M. Brecht (Humboldt University, Berlin) as well as A.M Oswald and S.M Sherman (both University of Chicago) for crucial feedback on the manuscript. We thank S.R. Postlewaite and current and former Hansel lab members S.E. Busch, D. Huang and T.F. Lin for insightful discussions and comments on the manuscript.

Funding: This work was supported by a National Institutes of Health (NINDS) grants R21NS136954 (to C.H.) and NS094184 (to K.P.K. in the lab of S.M Sherman).

Author contributions:

Conceptualization: A.S., K.P.K., C.H.

Methodology: A.S. K.P.K., C.H.

Investigation: A.S., K.P.K.

Visualization: A.S., K.P.K.

Funding acquisition: C.H.

Project administration: C.H.

Supervision: C.H.

Writing – original draft: A.S., C.H.

Writing – review & editing: A.S., K.P.K., C.H.

Competing interests: Authors declare that they have no competing interests.

Data and materials availability: All data and code will be made available online.

Materials and Methods

Animals

All experimental and surgical procedures were in accordance with the University of Chicago Animal Care and Use Committee guidelines. Mice were housed on a 12-hour light/dark cycle and fed a standard rodent diet. Animals of either sex were used in all experiments and no sex-dependent differences were observed in any reported measures. Strains included wildtype mice (C57BL/6J; Jax: 000664), PVCre mice (B6.129P2-Pvalbtm1(cre)Arbr/J; Jax: 017320), SSTCre mice (STOCK Ssttm2.1(cre)Zjh/J; Jax: 013044), VIPCre mice (B6J.Cg-Viptm1(cre)Zjh/AreckJ; Jax: 031628), and Ai9 mice (B6.Cg-Gt(ROSA)26Sortm9(CAG-tdTomato)Hze/J; Jax: 007909). Homozygous SSTCre, PVCre, and VIPCre animals were bred with wild type animals to generate heterozygotes. To generate SST and VIP reporter lines ($SSTCre^{tdTom}$ and $VIPCre^{tdTom}$), homozygous SSTCre and VIPCre mice were bred with homozygous Ai9 mice. Only heterozygous animals were used for experiments given evidence that endogenous somatostatin (SST) and vasoactive intestinal polypeptide (VIP) expression may be reduced in homozygous SSTCre and VIPCre animals, respectively (*76, 77*).

Stereotactic injections

For electrophysiological experiments. Stereotactic virus injections for electrophysiological experiments were performed as previously described using C57BL/6J mice between postnatal day 23-28 (*78*). For optogenetics experiments in which cerebellar inputs to zona incerta were measured, a 250 nL (40 nL/min) infusion of AAV5-hSyn-hChR2(H134R)-EYFP (UNC Vector Core) was made into the right deep cerebellar nuclei (-1.5 ML; -5.8 AP; -3.2 DV, *79*) using a 1 mL Hamilton syringe (catalog: 65458-02) with a flat needle tip. Next, a small infusion (40 nL total, at 7nL/min) of fluororuby (ThermoFisher, catalog: D1817) was made into left posterior medial thalamus using a 0.5 mL Hamilton syringe (catalog: 65457-01). Following a two-week incubation, animals were sacrificed for recordings in acute slices (see *Slice electrophysiology*).

For tracing experiments. For anterograde transsynaptic labeling experiments, a dual-injection approach was utilized to specifically label the outputs of neurons in the zona incerta that receive input from the contralateral cerebellar nuclei. Flpo-recombinase (pAAV-EF1a-Flpo, item#: 55637, Addgene) was injected into left deep cerebellar nuclei as above (+1.5 ML; -5.8 AP; -3.2 DV), followed by an infusion of AAV1-Flp-on ChR2-EYFP (AAV-hSyn-Coff/Fon-hChR2(H134R)-EYFP-WPRE, UNC Vector core) into right zona incerta (-1.8 ML; -2.0 AP; -4.0 DV). Following a 5-week incubation – the period required for anterograde transport of the AAV1 virus injected into zona incerta – animals were transcardially perfused for histology (see *Tissue preparation for fluorescence microscopy and immunohistochemistry*).

To visualize potential overlap between cerebellar terminals and cells in thalamic nuclei (i.e., the thalamic reticular nucleus) that project to somatosensory thalamus (ventral posteromedial nucleus and posterior medial thalamus), an orthograde virus (AAV5-hSyn-hChR2(H134R)-EYFP (UNC Vector core)) was injected into the right deep cerebellar nuclei (-1.5 ML; -5.8 AP; -3.2 DV) and fluorogold (2% w/v in sterile saline, Fluorochrome) was injected into the left somatosensory thalamus (primarily posterior medial thalamus). Following a 2-week incubation, animals were transcardially perfused for histology (see *Tissue preparation for fluorescence microscopy and immunohistochemistry*).

For two-photon calcium imaging experiments. Viral injections were performed to express channelrhodopsin-2 in cerebellar climbing fibers; fluorescent calcium indicators in cerebellar Purkinje cells or primary somatosensory (S1; barrel) cortex neurons; tdTomato, activating DREADDs, or inactivating DREADDs in S1 cortex; and inactivating DREADDs in interneurons in zona incerta. With respect to the inferior olive injection site (conferring viral expression in climbing fibers terminating in the contralateral cerebellar hemisphere), injections into cerebellar cortex were performed contralaterally, and injections into zona incerta and somatosensory cortex were performed ipsilaterally.

To express channelrhodopsin-2 in cerebellar climbing fibers ChR2-EYFP (AAV9-CaMKIIa-hChR2(H134R)-EYFP; Addgene #26969-AAV9) or ChR2-mCherry (pAAV-CaMKIIa-hChR2(H134R)-mCherry; Addgene #26975-AAV9) was injected into the left inferior olive as follows: after surgical preparation (see *Two-photon calcium imaging: Cranial window surgeries*), tissues attached to the occipital bone were surgically detached, followed by opening of the posterior atlanto-occipital membrane to expose the dorsal medulla. A 5µL Hamilton Neuros syringe (catalog: 65460-03) with a 33-gauge beveled needle tip (catalog: 65461-02) was inserted into the left medulla at an angle of 58-59° to the perpendicular line (Figure S2.A), 0.75 mm laterally and 1.70 mm deep from the surface of the medulla as previously described (*80*). A total volume of 400 nL was infused at a rate of 80 nL/min, and the syringe was held in place for five minutes before removal. ChR2-EYFP or ChR2-mCherry was chosen based on the excitation and emission spectra of other fluorophores expressed in the same animal to maximize signal separation when conducting post-hoc confocal imaging.

Stereotactic virus injections for imaging of Purkinje cell dendrites were administered as previously described using P80-120 adult C57BL/6J mice (*64*). A virus mixture was prepared with 0.5% L7-Cre (AAV1.sL7.Cre.HA.WPRE.hGH.pA, Princeton Neuroscience Institute Viral Core Facility, kindly provided by the lab of Dr. Samuel Wang at Princeton University), and 20% Cre-dependent GCaMP6f (AAV.CAG.Flex.GCaMP6f.WPRE.SV40; Addgene, #100835) in saline solution. A glass pipette with a tip diameter of ~300 µm was prepared by a puller (model P-97, Sutter Instrument Co.) and used to inject a total volume of 1800 nL into two separate injection sites: 900 nL were injected into right medial Crus I (-1.8 ML; -7 AP; -1.8 DV), followed by a 900 nL injection into right medial Crus II (-2.5 ML; -7 AP; -2.2 DV). The pipette carrying the AAV virus was held in place for five minutes before withdrawal.

For DREADD suppression of PV interneurons in zona incerta, a 1 mL Hamilton syringe was used to infuse Cre-dependent hm4D(Gi) (AAV1-hSyn-DIO-hM4D(Gi)-mCherry; Addgene #44362-AAV1) into the left zona incerta (1.8 ML; -2.0 AP; -4.0 DV) of PVCre animals.

To express GCaMP6f in primary somatosensory (barrel) cortex neurons in C57BL/6J, SSTCre^{tdTom}, and VIPCre^{tdTom} animals, a 5µL Hamilton Neuros syringe with a 33-gauge beveled needle tip (the same model used for inferior olive injections) was used to infuse a total volume of 800 nL of GCaMP6f (AAV1.Syn.GCaMP6f.WPRE.SV40; Addgene #100837-AAV) at two separate injection sites: 400 nL were injected at -1.2 AP; 2.5 ML and 400 nL at -1.5 AP; 3 ML. At each injection site, 200 nL were first injected 300 µm below the pial surface, followed by 200 nL at 150 µm below the pial surface. The injections were performed at a rate of 100nL/minute, and the syringe was held in place for five minutes before removal. To express GCaMP6f in barrel cortex neurons with co-expression of tdTomato in parvalbumin (PV)-, SST-, and VIP-expressing interneurons in PVCre, SSTCre, or VIPCre animals, respectively, GCaMP6f (Addgene #100837-AAV1) and Cre-dependent tdTomato (AAV9-FLEX-tdTomato; Addgene #28306-AAV9) were co-injected using the same technique. To optimize co-expression of the

viruses, GCaMP6f with tdTomato was mixed at a 3:1 volume ratio. For DREADD activation or suppression of VIP and SST interneurons, Cre-dependent hM3D(Gq) (AAV1-hSyn-DIO-hM3D(Gq)-mCherry; Addgene #44361-AAV1) or Cre-dependent hM4D(Gi) (AAV5-hSyn-DIO-hM4D(Gi)-mCherry; Addgene #44362-AAV5) were used in place of tdTomato, respectively.

For all two-photon imaging experiments, recordings began after a 4-week incubation period after the final virus injection (see *Two-photon calcium imaging: cranial window surgeries for detail*).

Tissue preparation for fluorescence microscopy and immunohistochemistry

After completion of two-photon experiments, selected animals (all those used in DREADD and cerebellar imaging experiments, and a subset of animals in all other experimental cohorts) were transcardially perfused with ice-cold 4% paraformaldehyde in phosphate-buffered saline (25mL), pH 7.4. The brain was extracted and postfixed in 4% paraformaldehyde overnight at 4°C before being transferred to a cold 30% sucrose (in phosphate-buffered saline) solution for >48 hours. Brains were then cryosectioned at 50 µm thickness, with an approximately equal number of brains sectioned coronally or sagittally per experimental cohort. For tracing experiments, animals were perfused with ice-cold phosphate-buffered saline (25mL) prior to perfusion with paraformaldehyde and cryosectioned coronally at 150 µm thickness. Slices were stored in phosphate-buffered saline prior to immunohistochemistry or confocal imaging.

For post-hoc visualization of Purkinje cells in mice expressing ChR2-EYFP in climbing fibers (i.e., in animals without GCaMP6f expression in Purkinje cells), calbindin immunohistochemical staining was performed. Tissue slices were washed in a 0.01M phosphate-buffered saline solution containing 200 mM glycine for two hours at 4°C, then incubated in a 0.01M phosphate-buffered saline solution containing 10 mM sodium citrate and 0.1% Tween-20 at ~60°C for 30 minutes using a heated water bath. After cooling to room temperature, the slices were washed three times in a 0.01M phosphate-buffered saline solution containing 0.5% Tween-20 (PBS-Tween) at room temperature for a period of 15 minutes per wash. Tissue was permeabilized with 200 mM glycine in PBS-Tween for 15 minutes at room temperature. Blocking was done for two hours at room temperature with a PBS-Tween solution containing 5% bovine serum albumin and 10% normal donkey serum, followed by overnight incubation (12-15 hours) at 4°C in a PBS-Tween solution containing 1% normal donkey serum and guinea pig anti-calbindin primary antibody (1:500; Synaptic Systems Cat# 214 004, RRID:AB_10550535). After washing the tissue three times for fifteen minutes in PBS-Tween at 4°C, slices were incubated for two hours at 4°C in PBS-Tween containing 1% normal donkey serum and donkey anti-guinea pig Cy3 (555) secondary antibody (1:200; Jackson ImmunoResearch Labs Cat# 706-165-148, RRID:AB_2340460). Finally, the slices were washed three times in PBS-Tween (ten minutes per wash) before mounting with Vectashield (Vector Laboratories, Inc.). The mounted slices were allowed to set overnight before imaging.

To confirm the channelrhodopsin-2 expression observed in cerebellar cortex was indeed expressed in climbing fiber terminals, a subset of tissue was additionally labeled with VGluT2. VGluT2 (rabbit anti-VGluT2, 1:500; Thermo Fisher Scientific Cat# 42-7800, RRID:AB_2533537*)* was added to the primary antibody solution and donkey anti-rabbit AF647 (Jackson ImmunoResearch Labs Cat# 711-605-152, RRID:AB_2492288) was added to the secondary antibody solution.

Confocal imaging

Image acquisition. Z-stack confocal images were taken at 5x (Olympus MPlan N 0.1NA, air), 10x (Zeiss Achroplan 0.25NA, air), 20x (Olympus UMPlanFL N 0.5NA, water), 40x (Zeiss EC Plan-Neofluar 1.3NA, oil immersion), and 63x (Zeiss W Plan-Apochromat, water) magnifications with a Zeiss LSM 900 Axio Examiner.Z1 scope. A subset of images (Figure 1.E and Figure S1.B) were taken with a Zeiss LSM 5 Exciter, Axioskop 2 (using the 20x Olympus UMPlanFL and 40x Zeiss EC Plan-Neofluar objectives, respectively). The images in Figure 5.D (shown with channel separation in S8.B) and S7 were taken with a second Zeiss LSM 900 confocal microscope. To facilitate direct comparison, images shown in series (as in Figure 5.C and Figure S6.F) were taken with identical hardware and software configurations, available in the image metadata.

Post-hoc image processing. To stitch multiple images (as in Figures 1.B, 1.D, 2.D-F (right), 4.B, 4.F, 5.B, 5.C, S1.A (top), S1.E, and all in S6), a series of pairwise stiches were performed using Fiji (NIH). Figures 1.B and S1.A (top) each consisted of 4 images (each 5x magnification, 1024 x 1024 pixels). Figure 1.D consisted of 12 images (each 5x magnification, 512 x 512 pixels). Figure 2.D (right) consisted of 10 images (each 10x magnification, 1024 x 1024 pixels). Figures 2.E and 2.F (right) each consisted of 8 images (each 10x magnification, 512 x 512 pixels). Figures 4.B and 4.F each consisted of 2 images (each 20x magnification, 512 x 512 pixels). Figure 5.B (also shown as the first image in S6.F) and all images in S6.F each consisted of 6 images (each 5x magnification, 512 x 512 pixels). Images in 5.C each consisted of 9 images (each 10x magnification, 512 x 512 pixels). Figure S1.E consisted of 8 images (each 5x magnification, 1024 x 1024 pixels). Images in S7.A (bottom) and S7.B (top and bottom left) each consisted of 6 images. Note a subset of the final images displayed in figures are cropped to show relevant detail.

Channel colors set during image acquisition followed conventional emission wavelength assignments (i.e., red to indicate tdTomato, green to indicate GCaMP6f, etc.). To illustrate interneuron subtypes and continuity across experiments (e.g., cyan to indicate ChR2 expression in optogenetic stimulation experiments), channel colors were specified post-imaging using Fiji by separating channels and selecting the appropriate color when merging, ignoring source LUTs. When necessary, post-hoc brightness and contrast adjustments were applied linearly to an entire image – *after* stitching, if applicable – using Fiji. To facilitate direct comparison, identical linear brightness/contrast adjustments were made across all images shown in series (as in Figures 5.C and S6.F).

To measure terminal density across the sections shown in Figure 5.C, Fiji was used to rotate each image such that the axis separating ventral from dorsal zona incerta was horizontal. A 400 µm x 1 mm region of interest (ROI) was drawn around the zona incerta, and each row of pixels within this ROI was separated to facilitate calculation of the integrated density across each row of pixels. A similar method was used to quantify the terminal density of cerebellar inputs to zona incerta as in Figure S8.C. Briefly, images of sections matched for their rostro-caudal location were rotated as before. Then, five line-ROIs oriented vertically, each being 200 µm wide, were positioned side-by-side across the mediolateral axis of the zona incerta, and the spatial pattern of fluorescence along these lines was measured by calculating the mean grey value along their length (which was roughly 400 µm from the dorsal boundary to the ventral boundary). These were averaged for each animal used. Shading represents SEM for both measurements.

Slice electrophysiology

Acute slice preparation and whole cell recordings. For recordings in acute slice, injected animals (see *Stereotaxic injections: For electrophysiological experiments*) were deeply anesthetized using the isoflurane drop method in a bell jar (with a raised platform for the animal) and immediately transcardially perfused with 8-10 mL of ice cold oxygenated (95% O2, 5%CO2) artificial cerebrospinal fluid, which contained the following (in mM): 125 NaCl, 25 NaHCO3, 3 KCl, 1.25 NaH2PO4, 1 MgCl2, 2 CaCl2, and 25 glucose. The brain was then extracted, glue-mounted on a vibratome (Leica) platform and blocked for coronal slices using an agarose (5%) cube and sliced in the same solution (ice-cold). Slices were cut to 365 µm thickness. The brain slices were then transferred to 32-34 °C oxygenated artificial cerebrospinal fluid that was allowed to return to room temperature over the course of one hour, which constituted the slice recovery period.

Slices containing the zona incerta and terminals from the cerebellar nuclei inputs were visualized using differential interference contrast with an Axioskop 2FS microscope (Carl Zeiss). Fluorescence from ChR2-EYFP expression and from retrograde fluororuby labeling was confirmed using the 5x air objective and guided recording locations in zona incerta. Recordings were made with a Multiclamp 700B amplifier and pCLAMP software (Molecular Devices). Recording glass pipettes with 7–9 MΩ resistance were filled with an internal solution as follows (in mM): 117 K-gluconate, 13 KCl, 1 MgCl2, 0.07 CaCl2, 10 Hepes, 0.1 EGTA, 2 Na2-ATP, 0.4 Na-GTP, pH 7.3, 290 mOsm. Incertal cells whose morphology was clearly revealed by strong red fluorescence, indicating retrograde labeling from posterior medial thalamus, were targeted for recordings. Bath application of TTX (1 µM) was performed in a subset of recorded cells to verify the monosynaptic nature of the cerebellar input to zona incerta.

Optogenetic stimulation was delivered using a 355 nm laser (DPSS: 3505–100), controlled with galvanometer mirrors (Cambridge Technology) focused on the slice through a 5x air objective using custom software in MATLAB (MathWorks). Focal photostimulation of the ChR2-expressing synaptic terminals in zona incerta was performed at 10Hz (4 pulses of 1-ms duration at 100 ms interstimulus interval).

Electrophysiological data analysis. Electrophysiological data were collected using custom MATLAB software and analyzed using Graphpad Prism (v7.0). The amplitude of excitatory responses (i.e., the first response in the stimulus train) to stimulation pulses was measured by subtracting the average value for 20 ms before the delivery of a pulse (baseline) from the maximum value of the peak in current clamp at resting membrane potential. Latency of the optogenetic response was calculated by measuring the delay in milliseconds from the onset of the first optogenetic stimulus to the moment the resulting response reached >10% of its maximum amplitude.

Two-photon calcium imaging

Cranial window surgeries for imaging of Purkinje cell dendrites. To minimize overall recovery burden, surgeries were performed in two stages: (1) inferior olive virus injection and headframe installation, and (2) cerebellar virus injection and cerebellar cranial window installation as previously described (*65*). In the first stage, mice (P60-90) were deeply anesthetized using 1-2% isoflurane and clamped by ear bars at the external acoustic foramen. The line between the clamping point and maxilla was set parallel to the horizontal plane. After

trimming the fur on top of the skull with clippers, the surgical site was prepared by applying betadine and 70% ethanol three times in an alternating fashion. Meloxicam (2 mg/kg), extended-release buprenorphine (0.1 mg/kg), and 0.5 mL saline were administered subcutaneously, and depth of anesthesia was confirmed via tactile stimulation of the toe before making a 20-25 mm incision in the skin to reveal the occipital bone and attached tissues. After opening of the posterior atlanto-occipital membrane and channelrhodopsin-2 virus injection into the left inferior olive (see *Stereotaxic injections: For two-photon calcium imaging experiments*), tissues were reattached to the occipital bone using instant adhesive, ensuring adequate space for later implantation of the cranial window over the right cerebellar cortex. A custom titanium headframe (H. E. Parmer Company, Nashville, TN, USA) was secured with dental cement (Stoelting Co., Wood Dale, IL, USA), completing the first stage.

After monitoring recovery for a period of 4 days, mice underwent the second surgery. A circular craniotomy over right cerebellar cortex with a diameter of 4mm, centered at -2.7ML; -6.9 AP, was performed using a dental drill. The dura was carefully removed to expose lobules Crus I and anterior Crus II before administering GCaMP6f injections (see *Stereotaxic injections: For two-photon calcium imaging experiments*). Following injection, a two-layer glass window was installed using C&B Metabond dental cement (Patterson Dental Company, Saint Paul, MN, USA), completing the second stage. The glass windows consisted of a 4 mm glass window (Tower Optical Corp, Boynton Beach, FL, # 4540-0495) adhered to a 5 mm glass window (Warner Instruments, Holliston, MA, USA, # CS-5R) using ultraviolet light-activated glue (Norland Optical Adhesive 71; Norland Products Inc., Jamesburg, NJ). Experiments were conducted 4.5 weeks after inferior olive injection and 4 weeks after GCaMP6f injection.

Cranial window surgeries for imaging of barrel cortex neurons. Surgeries were again separated into two stages: (1) inferior olive virus injection, headframe installation, and cerebellar cranial window installation; and (2) S1 cranial window installation and virus injection. First, channelrhodopsin-2 was injected into the left inferior olive as above (see *Cranial window surgeries for imaging of Purkinje cell dendrites* and *Stereotaxic injections: For two-photon calcium imaging*). After reattaching tissues to the occipital bone using instant adhesive, a dental drill was used to perform a circular craniotomy over right cerebellar cortex (lobules Crus I and II), followed by removal of the dura and installation of the glass window as above. Finally, the custom titanium headframe was secured using dental cement, completing the first stage.

After monitoring recovery for a period of 4 days, mice underwent the second surgery. After surgically detaching a small portion of the left temporalis muscle attached to the parietal bone, a second circular craniotomy over left primary somatosensory cortex with a diameter of 4 mm (centered at -1.5 AP; 3 ML) was performed. The dura was removed to expose the neocortical surface before administering the appropriate viral injections (see *Stereotaxic injections: For two-photon calcium imaging experiments*). Following injection, a glass window was installed over the craniotomy using dental cement. To ensure optical isolation during recordings, a custom sheath was used to couple a Thorlabs patch cable (used for LED stimulation of cerebellar climbing fibers; see *Optogenetic and tactile stimulation*) to the cerebellar window. This sheath was adhered over the cerebellar window using Metabond dental cement, completing the second stage. For experiments involving DREADD manipulation of neurons in zona incerta, viral injections into left zona incerta were administered three days prior to the first surgery. Thus, experiments were conducted approximately 5 weeks after zona incerta injection, 4.5 weeks after inferior olive injection, and 4 weeks after primary somatosensory cortex injections.

Habituation. After completion of surgeries, postoperative care was provided for 5-7 days. Once animals exhibited exploratory behavior without signs of pain or distress, habituation began with handling of mice for 15 minutes and transportation from the animal facility to the laboratory. After two days, anxiety during handling typically diminished, and the handling period increased to 30 minutes in the vicinity of the recording area. Following two days of handling, the mice were introduced to a free-running treadmill and head restraint via clamping of the head frame on left and right sides. The duration of time spent on the treadmill increased from 10 minutes to two hours per day depending on the mouse's comfort. The relative time spent running on the treadmill typically decreased after two days. To habituate mice to air puff stimulation during this time, receptive field mapping of the field of view was conducted by delivering 8psi air puffs through a capillary tube while observing epifluorescence signals and calcium responses in real time. Air puffs were delivered at irregular frequencies, with at least 30 seconds between stimuli, to avoid influencing subsequent plasticity experiments. In total, mice were habituated for a period of 1-2 weeks until they showed no aversive responses to air puff stimulation, spent the majority of time in the recording environment at rest, and reduced movement initiation (whisking/running) with air puff stimulation. Animals used for DREADD manipulation experiments were familiarized with the DCZ injection procedure by receiving DMSO/saline injections during habituation for two days prior to recording.

Optogenetic and tactile stimulation. To optogenetically stimulate cerebellar climbing fibers, the tip of a Ø200 µm core rotary joint patch cable (Thorlabs catalog: RJPSL2) was inserted into the sheath attached to the cranial window over the right cerebellar cortex (see *Two-photon calcium imaging: Cranial window surgeries*). Blue light pulses were delivered with a 470 nm Fiber-Coupled LED (Thorlabs catalog: M470F3). To deliver whisker stimuli, a 0.86 mm diameter glass capillary tube was positioned over the right C-row whiskers 5 mm from the right whisker pad at an angle of 45° in the X and Y planes (adjusted slightly during receptive field mapping for each animal). Air puffs were delivered at 8 psi (Picospritzer III, Parker Hannifin). For all imaging sessions, calcium activity was measured in trials lasting 20 seconds, with a stimulus delivered once per trial. Trials began at random intervals, with an interval of at least 5 seconds between trials. When testing Purkinje cell responses to optogenetic climbing fiber stimulation, 470 nm pulses were delivered with the following durations: 1 x 20ms, 1 x 50ms, 3 x 15 ms at 8 Hz, and (3 x 15 ms at 8 Hz)*2 with a 250 ms interval between epochs (Figure S1). The 1 x 50 ms light pulse was selected for all subsequent experiments. To test the basic transmission of the climbing fiber signal to S1 (i.e., the immediate influence of optogenetic stimulation of climbing fibers on whisker responses shown in Figure 2), 100 ms air puffs were delivered with or without optogenetic co-stimulation of climbing fibers. For paired stimuli, the 50 ms blue light stimulus was delivered with a delay of 45 ms with respect to the onset of the whisker stimulus. This delay was chosen to mimic the natural latency of climbing fiber responses to whisker stimulation, which peaks approximately 50 ms after stimulus onset (*54*). For plasticity experiments, whisker test pulses were delivered during a baseline period of at least 30 minutes, followed by a 5-minute period of rhythmic whisker stimulation (RWS) at 8 Hz – the speed at which mice naturally sample objects (*39*). After plasticity induction, test pulses were delivered for a period of at least 40 minutes. For plasticity experiments with optogenetic co-activation of climbing fibers (RWS+CF), the same protocol was followed with the addition of 50 ms blue light pulses at 1 Hz during plasticity induction. To coordinate precise stimulus delivery, a Cygnus Digital Stimulator (catalog: PG4000A, Cygnus Technology, Inc.) was interfaced with an Arduino Uno to trigger both the LED driver and picospritzer.

Cerebellar imaging protocol. Calcium imaging of the genetically encoded indicator GCaMP6f was conducted in Crus I/II of the right hemisphere of awake, head-fixed mice using a laser scanning two-photon microscope (Neurolabware, Los Angeles, CA, USA) and Scanbox software (Scanbox, Los Angeles, CA). Calcium images were obtained at a frame rate of 30.98 fps with a pixel dimension of 512 x 796, using an 8KHz resonant scanning mirror with bidirectional scanning. A Mai Tai® DeepSee (Spectra-Physics, Milpitas, CA, USA) laser source was used to excite GCaMP6f at 920 nm. The fluorescence emission was collected through a 16x water-immersion objective (Nikon LWD 0.8NA, 3 mm WD) using a GaAsP PMT (Hamamatsu Photonics, Shizuoka, Japan). A 2.0 or 2.8x digital zoom was applied during imaging, generating a field of view of 760 x 613 or 551 x 444 µm, respectively. To minimize background noise originating from ambient light, a custom light shield was fitted around the brain window and objective. This shield had a small opening such that the Thorlabs patch cable used for LED stimulation of climbing fibers could be positioned over the cerebellar window. The laser power was set to 1% with a PMT gain between 0.79 and 0.81, allowing for prolonged recording while minimizing phototoxicity.

S1 imaging protocol. Calcium imaging of GCaMP6f was conducted in barrel cortex of the left hemisphere using the same hardware as above. Images were obtained at a frame rate of 30.98 Hz with a pixel dimension of 512 x 796. A 2.4x digital zoom was applied during imaging, generating a field of view of 638 x 515 µm. Two of 11 RWS+CF experiments and one of 10 RWS experiments were conducted using a 2.0x digital zoom (generating a field of view of 760 x 613 µm) and were added to the experimental cohorts, as results were not significantly different across any reported measures. A custom light shield was fitted around the brain window and objective to reduce background noise originating from ambient light. Note further isolation of the LED light used for optogenetic stimulation of climbing fibers was provided by the sheath attached to the cerebellar window (see *Cranial window surgeries for imaging of barrel cortex neurons*). While observing the epifluorescence signal, small vessels on the putative surface of the brain were put into focus in the z plane and matched to a field of view selected during receptive field mapping (see *Habituation*). After adjusting the focus 250 µm below the putative pial surface, small adjustments were made in the x-y planes while observing calcium signal in real time to maximize responsivity to whisker stimulation and overlap between GCaMP6f and tdTomato or mCherry in the field of view. GCaMP6f was excited at 920 nm and tdTomato or mCherry (for DREADD experiments) at 1040 nm, with emitted fluorescence collected using two GaAsP PMTs. The laser power was set to 2%, and adjustments to the PMT gain were made due to slight variance in the level of GCaMP6f and tdTomato/mCherry signal across animals. PMT gain in the green channel was 0.73 (SD: 0.07) while PMT gain in the red channel was 0.83 (SD: 0.14), which were not significantly different across experimental groups. Responsivity to whisker stimulation was determined by intermittently delivering 8 psi air puffs at random intervals, with a minimum of 30 seconds between stimuli, to avoid influencing plasticity experiments. If more than ten minutes were spent determining an optimal field of view on the day of recording, the experiment was aborted and instead conducted the following day. Mice were occasionally used for multiple recording configurations but were sacrificed immediately after performing plasticity experiments, and selected animals were used for histological characterization (see *Tissue preparation for fluorescence microscopy and immunohistochemistry*). Note DREADD expression was histologically verified in all animals to ensure expression was restricted to neocortex.

DREADD experimental protocol. To activate the hM4D(Gi) and hM3D(Gq) receptors, we used deschloroclozapine dihydrochloride (DCZ, MedChemExpress), which was chosen over

clozapine N-oxide (CNO) as an agonist due to its heightened selectivity for hM4D(Gi) and hM3D(Gq) receptors over endogenous receptors, a more rapid onset than CNO, and significantly increased potency. DCZ was dissolved in DMSO at a 0.02 mg/mL concentration and stored at −80 °C. On the day of recording, DCZ aliquots were thawed to room temperature and diluted to 0.01 mg/mL with DMSO/saline. Two-photon calcium imaging experiments began with recordings of baseline responses to whisker stimulation (with and without optogenetic stimulation of climbing fibers in a subset of experiments), followed by an injection of DCZ (0.1 mg/kg) intraperitoneally. Injections were carefully administered to ensure the field of view would not be disturbed (experiments were aborted if this occurred, as responses in each period could no longer be directly compared). Activation of receptors was allowed to take effect for fifteen minutes prior to resumption of recording, after which a second period of baseline activity was recorded. This period lasted between fifteen and thirty minutes, such that a period of fifteen minutes of stable activity was recorded prior to plasticity induction. Plasticity induction protocols were followed as above (see *Optogenetic and tactile stimulation*), and whisker test pulses were delivered for at least 40 minutes after plasticity induction. To ensure observed plasticity phenomena were not the result of prolonged changes in activity related to hM4D(Gi) or hM4D(Gq) activation, control experiments lasting the same duration as the plasticity experiments were conducted similarly, except without induction of plasticity (see Figure S5.A, S5.D, S5.G, and S5.J, right). To ensure DREADD expression was localized to the neocortex, expression was confirmed histologically (see *Tissue preparation for fluorescence microscopy and immunohistochemistry*).

Characterization of neurons. Calcium images taken in the green (PMT0) and red (PMT1) channels were first merged, trial-averaged, and concatenated using Fiji. The average image was then calculated, followed by identification of all cells expressing tdTomato or mCherry (applicable to all recordings except the zona incerta manipulation experiments). ROIs were manually drawn around each cell co-expressing GCaMP6f and tdTomato or mCherry. All images across a session were then concatenated and trial-averaged before calculating the maximum image. ROIs were manually drawn around all putative pyramidal neurons, which were identified with the following criteria: a triangular or pyramidal soma, the presence of a single apical dendrite extending in a similar orientation to other pyramidal cells in the same imaging session, and the presence of basal dendrites smaller in diameter than the apical dendrite. In a subset of experiments in which apical dendrites could not be clearly distinguished in the imaging plane, z-stack images were taken at the end of the imaging session, averaged, and referenced to visualize apical dendrites. After identification of fluorescently tagged interneurons and pyramidal neurons, relevant putative interneurons were morphologically identified and compiled (e.g., putative VIP and SST neurons in PV-tagged mice). Putative interneurons were identified by the presence of an elongated soma and bipolar dendritic arbors (likely VIP), round somas smaller in diameter than pyramidal cells, and neurons with multiple perisomatic dendrites (usually highly branched; likely PV). The morphology of untagged interneurons was visually compared to the morphology of tagged interneurons in relevant mice (e.g., morphologically identified interneurons in PVCre mice were compared to fluorescently tagged interneurons in SSTCre and VIPCre mice). The average (11.07µm, SD 1.64µm) and maximum (18.14µm, SD 2.74µm) soma diameter for morphologically identified pyramidal neurons ($n = 3358$) were significantly higher than in morphologically identified interneurons in the same mice ($n = 3522$; average: 9.90µm, SD 1.96; maximum: 16.37µm, SD: 3.39µm; $p < 0.001$ for both values, unpaired t-test) and tagged VIP, SST, and PV neurons ($n = 543$; average: 8.96µm, SD 1.87µm; maximum: 14.98µm, SD 3.51µm; $p < 0.001$ for both values, unpaired t-test).

Intrinsic Signal Imaging

Image acquisition. Mice underwent the same surgical procedures described in *Two-Photon calcium imaging: Cranial window surgeries for imaging of barrel cortex neurons.* To facilitate manipulation of single whiskers, mice were lightly anesthetized with 10 mg/kg ketamine and placed on a stereotaxic frame. Using a custom GUI written in MATLAB, small vessels were visualized under a green LED (525 nm wavelength) with a high-speed camera (Teledyne DALSA Genie Nano GigE). Focus in the z-plane was adjusted approximately 250 µm below the putative pial surface before taking a reference image of the vasculature. For measurement of intrinsic signals, the field of view was illuminated with red light (625 nm). An Arduino Uno and MATLAB were used to trigger trial onset, the device used to mechanically deflect whiskers (a glass capillary tube attached to a rotary motor), a blue LED to stimulate climbing fibers, and recording of intrinsic signals at 30 Hz. Trials consisted of a 1-second baseline period, followed by a 1-second test pulse in which whiskers contralateral to the optical window were mechanically deflected at 8 Hz (RWS). This was repeated with an inter-trial interval of 18 seconds for 30 minutes prior to plasticity induction, after which whiskers were stimulated at 8 Hz for 5 minutes. Test pulses were delivered for 40 minutes after plasticity induction. For RWS+CF and control experiments, 50 ms blue light pulses were delivered at 1 Hz during plasticity induction with or without 8 Hz co-stimulation of whiskers, respectively.

Image processing. Evoked signals were calculated similarly to Vasquez *et al* (*81*). Briefly, images were smoothed with a Gaussian filter and spatially downsampled by a factor of four. For each trial, an average baseline reflectance image (R0) was generated by calculating the average across the 1-second (30 frame) period before stimulus onset. Post-stimulus reflectance images were temporally averaged across 200 ms bins for 600 ms total, starting 400 ms after stimulus onset. The change in reflectance, $\Delta R/R$, was calculated by subtracting R0 from each post-stimulus image and dividing the result by R0. Each of the three bins (400-600 ms, 600-800 ms, and 800 ms-1 s post stimulus onset) were averaged across a minimum of 30 trials and finally summed to yield a single total stimulus-evoked $\Delta R/R$ image. The reference image taken with green light illumination was used to draw a region of interest around the cranial window. Pixels outside this ROI mask were set to zero. Binary images were generated by calculating z-scores of the $\Delta R/R$ image and thresholding values below a z-score of -1.5 (note negative changes in reflectance indicate an increase in the presence of deoxyhemoglobin caused by increased oxygen consumption by active neurons). Binarized images were overlaid onto reference images. To calculate the areal extent of single whisker-evoked responses, clusters of active pixels were identified by applying a median filter with a 5 x 5-pixel neighborhood size, and the number of pixels above threshold was calculated. To reduce the impact of residual noise (i.e. detected pixels outside the area reliably activated by a single whisker), values were normalized by the area of the cranial window.

Two-photon image processing

Processing of cerebellar data. Processing of Purkinje cell calcium traces was conducted as previously described (*65*). Individual trials from each session were concatenated along the z-axis, representing a time series across the entire recording session, to ensure consistency among trials after motion correction. The concatenated file underwent motion correction using a custom MATLAB script (MATLAB R2017b, MathWorks, Natick, MA, USA) based on whole frame

cross-correlation (provided by the lab of Mark Sheffield, University of Chicago). Cellular regions of interest were manually selected in Fiji based on the average field of view across trials. Trials were then separated for further processing. In a subset of trials, optogenetic stimulus artifacts were visible in a portion of the field of view in 1-3 nonconsecutive frames, depending on the stimulus duration. These frames were manually identified and excluded using Fiji before further processing.

Using custom MATLAB script, ΔF/F values were calculated from the raw trace using the following equation: (Ft − F0)/F0, where Ft represented the raw calcium intensity of the time series, and the baseline fluorescence (F0) was set as the 20th percentile of the fluorescence trace from each trial. ΔF/F values were then subjected to low-pass filtering using a five-frame moving window smoothing function. Finally, traces were normalized to a pre-stimulus baseline period by subtracting the average ΔF/F value from the 5-frame period prior to stimulus onset from the entire trace. To visualize population average responses to optogenetic stimulation of climbing fibers, calcium signals from each ROI were first trial-averaged, followed by concatenation and averaging of the signal across cells and mice. To calculate maximum amplitude of responses in the evoked period, the maximum in a window 0-700 ms after stimulus onset was calculated for each ROI's trial-averaged trace, then concatenated across cells and mice. Area under the curve (AUC) was calculated similarly by integrating the ΔF/F values over the same window. To identify spontaneous events, frame indices in which the first and second derivatives of the ΔF/F signal reached 0.1 were identified (F^{idx}). Peaks were detected using a peak prominence threshold of 0.1 ΔF/F, with spontaneous events defined as peaks occurring within 200 ms of F^{idx} . The onset of each spontaneous event was determined as the frame in which the first derivative dropped below 0.05. A 1-second window following event onset was extracted. Finally, after averaging all detected spontaneous events within ROIs, spontaneous events were compiled across neurons to generate the population average trace.

Processing of S1 data. Motion correction and ROI curation were performed as above (see *Processing of cerebellar data* and *Two-photon calcium imaging: Characterization of neurons*). Residual optogenetic stimulus artifacts were observed in a single frame in a subset of trials, typically at or immediately after stimulus offset. These artifacts were detected using the *findpeaks* function in MATLAB and corrected by replacing the artifact frame's value with a linear interpolation of the two adjacent frames before further processing. Background subtraction was performed by calculating the bottom 1st percentile of the raw fluorescence trace collected from an ROI that did not contain cell bodies or neuropil, then subtracting this value from all trials. Smoothing, expression of raw signals as ΔF/F, calculation of baseline noise (σ), and calculation of the signal-to-noise ratio (SNR) were performed as in Ayaz *et. al.,* 2019 (*82*). Smoothing was performed with a 51-point 1st-order Savitsky-Golay filter, followed by calculation of the relative percent change of fluorescence ((Ft − F0)/F0) using the 1st percentile of the smoothed trace as F0. Given background subtraction prior to calculation of F0 may generate negative F0 values and subsequent signal inversion, ROIs with F0 < 0 were rejected from further analyses (44/7423 cells). To calculate σ for each neuron, a 5-second (155 frame) sliding window was first used to calculate the standard deviation of the fluorescence change during each 5-second period within a session. After compiling all values, the 1st percentile value was taken as σ. For each neuron, the SNR was defined as the 95th percentile of ΔF/F signals recorded across all trials divided by the baseline noise.

Evoked event detection. To detect stimulus–evoked events, we first applied OASIS deconvolution to the ΔF/F traces using an event detection threshold of 3σ to generate a binary

trace containing event times. An autoregressive model with order p=1 was used to ensure the number of events ("spikes") for each calcium transient varied with the amplitude of the calcium transient as previously observed (*40*). Next, for each frame, the sum of all events was calculated and divided by the number of trials to determine the proportion of trials with an event in a given frame (P^{event}). P^{event} was averaged across frames, and consecutive frames with P^{event} 3 standard deviations above the mean were selected. This generated an evoked event window of 387 ms (Figure S2.B). Finally, for each neuron, the calcium traces for all trials containing an event within the evoked event window were compiled for further analysis. To visualize population average traces for all experiments, evoked calcium signals for each neuron were first averaged across trials, followed by averaging across neurons. For visualizations between the same neural populations in different conditions, only those cells that responded to both conditions, i.e. having an evoked event in each condition, were included (following the definition of "Persistent cells" used in Williams *et. al.*, 2025, *45*). Shaded regions in population average traces represent SEM.

Calculation of amplitude and area under the curve in S1 recordings. For all calculations of AUC in S1 recordings, the ΔF/F signal was integrated over a 700 ms window after stimulus onset unless otherwise specified (details below).

To quantify plasticity phenomena caused by RWS or RWS+CF, all evoked events measured within 50 minutes prior to plasticity induction ("Pre") or 60 minutes after plasticity induction ("Post") were extracted for each cell and trial-averaged before calculating AUC. Only the neurons with evoked events both pre- and post-plasticity induction were included in subsequent analyses. AUC were averaged both across all neurons or within animal to perform statistics across neurons or mice (see *Statistics and quantifications*). To visualize the duration of plasticity effects, evoked events were binned into 10-minute epochs and trial-averaged within cells, followed by calculation of the AUC and averaging across neurons. To verify the robustness of plasticity effects, AUC and time course measurements were also analyzed across all cells and trials (i.e., those that did not meet evoked event criteria; Figure S.2) and in the absence of animal movement (Figure S3; see *Determination of active and rest trials*). To quantify plasticity phenomena in DREADD manipulation experiments, response amplitude was calculated in addition to AUC before and after plasticity induction. Response amplitude was taken as the maximum ΔF/F value in the same 700 ms window used for AUC calculations.

To quantify the immediate effect of climbing fiber activation on basic whisker responses in S1 cortex, AUC was calculated similarly for whisker stimulation (W) or whisker and CF co-activation (W+CF) trials. An additional measurement was taken 650-850 ms after stimulus onset for pyramidal neurons and VIP interneurons, as the effect of CF modulation was present in the later phase of the calcium response. Note that while W and W+CF test pulses were delivered prior to DCZ administration in DREADD experiments to verify functional opsin expression, these mice were excluded from this analysis due to an insufficient number of trials in each animal.

To verify that hM4D(Gi) and hM3D(Gq) expression in SST neurons indeed suppressed or increased their activity, respectively, AUC was calculated before and after DCZ administration in a window 1750 ms after stimulus onset. This larger window was used to capture the significantly increased duration of whisker-evoked calcium responses in SST neurons expressing hM3D(Gq). To verify that hM4D(Gi) and hM3D(Gq) expression in VIP neurons indeed suppressed or increased their activity, respectively, AUC was calculated before and after DCZ administration in a window 650-850 ms after stimulus onset. Given VIP neurons are modulated by climbing fiber stimulation in this phase of the calcium response (Figure 2.G), this later

window was chosen to ensure DREADD manipulation of VIP neurons suppressed or enhanced VIP responses in the physiologically relevant response period.

Determination of active and rest trials

Activity of mice was monitored at 30.98 Hz using a DALSA M640 CCD camera (Teledyne Technologies, Thousand Oaks, CA, USA) focused on the animal's face and a portion of the running wheel. To determine the frames in which mice were active, custom MATLAB script was used to generate a binary trace that indicated the frames in which movement between frames occurred (based on a comparison of pixel values between consecutive frames). For each recording session, movement traces and corresponding videos from ten randomly selected trials were manually inspected to ensure all frames in which mice were whisking or running were indicated. Note whisking occurred independently of running, but running seldom occurred without whisking. Rest trials were defined as any trial with no movement detected at least 400 ms before and after stimulus onset – longer than the evoked event window, and the same as the window chosen in Ayaz *et. al.,* 2019 (*82*) to distinguish rest from running onset. All other trials were considered active trials.

Statistics and quantifications

All statistics and quantifications were performed using MATLAB. To assess normality, we applied the Lilliefors test to each dataset before performing statistical calculations. For paired samples, a paired t-test was used when data were normally distributed, and a Wilcoxon signed-rank test was used for non-normal data. For unpaired comparisons, an unpaired t-test was used for normally distributed data, a Welch's t-test for normally distributed data with unequal variances, and a Wilcoxon rank-sum test for non-normal distributions. Categorical variables were compared using the Chi-squared test. Two-way ANOVA was used for multi-group comparisons (i.e., to determine whether plasticity effects across time were significantly different between groups). To perform statistics across all animals, average responses were first normalized by dividing the response in the relevant experimental condition by the baseline response. A one-sample t-test was then performed against a standard value of 1. Statistical significance was set to $p < 0.05$, with p values presented in figures as follows: $p < 0.05$: *; $p < 0.01$: **; $p < 0.001$: ***; $p > 0.05$: not significant (n.s.). Bar graphs represent mean ± SEM. Box plots contain the interquartile range (25th and 75th percentiles) and median.

Fig. 1. Optogenetic CF co-activation prevents adaptive L2/3 pyramidal cell potentiation in S1 cortex. (**A**) Experimental schematic for (**D** – **L**). (**B** and **C**) ChR2 expression in the inferior olive (IO) and optogenetic CF activation evokes calcium transients in PCs. (**B**) Calbindin staining of PCs marks the cerebellum (shown here in the same plane as the IO; white arrowhead). Scale bar: 1mm. (**C**) Top view of PC dendrites with calcium responses evoked by 470nm, 50ms LED pulses in PCs. Scale bar: 100µm. Right: Distribution of response amplitudes (box: 25th and 75th percentiles; line: median). (**D**) GCaMP6f expression in S1 cortex. Scale bar: 1mm. (**E**) Sagittal view of ChR2-expressing CF terminals in cerebellum that are activated in optogenetic experiments. Scale bar: 100µm. (**F**) Left: Example of the morphological identification of L2/3 pyramidal cells by apical dendrites (green arrowheads) and INs (white arrowheads). Scale bar: 100µm. Right: Pyramidal cell at higher magnification. Scale bar: 15µm. (**G**) Pyramidal cell plasticity after RWS (N=10 mice) and after pairing with CF activation (RWS+CF; N=11 mice). Right: Quantification of evoked responses across neurons. (**H**) Data in (**G**) binned across time. Blue shading: RWS/RWS+CF. (**I**) Quantification across mice, normalized to the average baseline whisker response. (**J**-**L**) Analyses for INs in the same mice. Data: mean ± SEM.

Fig. 2. Optogenetic CF co-activation differentially modulates basic responses to whisker stimulation in different types of neocortical neurons. (**A**) Schematic of the recording configuration (left) and S1 cortex microcircuit (right). (**B**) CF co-activation with whisker stimulation does not significantly alter response amplitudes in morphologically identified L2/3 pyramidal neurons (n=826 cells; N=23 mice) in the default analysis window (0-700ms; light shade), but responses decrease in the late response window (650-850ms; dark shade). Left: averaged traces. Middle: analysis by neuron. Shades distinguish analyzed time windows. Right: analysis by mouse (0-700ms). Blue line indicates mean. (**C**) CF co-activation significantly enhances responses in putative interneurons (INs; n=1104 cells; N=24 mice). (**D** – **F**) Sample two-photon field of view (left) and post-hoc verification of expression in S1 using confocal microscopy (right). Arrowheads indicate neurons co-expressing GCaMP6f and tdTomato in VIP interneurons (**D**), SST interneurons (**E**), or PV interneurons (**F**). Scale bars: 100µm (left); 500µm (right). (**G**) CF co-activation with whisker stimulation significantly reduces VIP population responses in the late analysis window (n=129 cells, N=7 mice; shades as in **B**), but enhances responses in SST interneurons (n=102 cells; N=12 mice; **H**) and PV interneurons (n=177 cells; N=18 mice; **I**). Middle plots show analysis by neuron, right plots analysis by mouse (blue line indicates mean). Scale bars: 0.1 ΔF/F; 0.5s. Data: mean ± SEM.

Fig. 3. SST interneurons are recruited to prevent L2/3 pyramidal cell plasticity. (**A**) Circuit diagram highlighting the chemogenetic activation of SST interneurons and recording configuration. (**B**) Expression of activating hM3D(Gq) receptors is localized to neocortical SST interneurons. Scale bar: 100µm (top) and 500µm (bottom). (**C**) DCZ application enhances responses in SST interneurons (n=12 cells; N=7 mice). (**D**) In the presence of DCZ, RWS stimulation suppresses L2/3 pyramidal cell potentiation, and even causes depression, even when the CF is not co-activated (n=255 cells; N=4 mice). Left: average traces; middle: analysis by cell (mean ± SEM); right: response range by cell (whiskers: range; box: 25th and 75th percentiles; line: median). (**E**) Circuit diagram highlighting the chemogenetic inhibition of SST interneurons and recording configuration. (**F**) Expression of inhibiting hM4D(Gi) receptors is localized to neocortical SST interneurons. Scale bars as in (**B**). (**G**) DCZ application reduces responses in SST interneurons (n=53 cells; N=6 mice). (**H**) In the presence of DCZ, pyramidal cell potentiation is observed, despite of CF-co-activation (n=183 cells; N=3 mice). Data analysis presented as in (**D**). Scale bars: 0.1 ΔF/F; 0.5s.

Fig. 4. VIP interneurons mediate the effects of optogenetic CF activation. (**A**) Circuit diagram highlighting the chemogenetic inhibition of VIP interneurons and recording configuration. (**B**) Expression of inhibiting hM4D(Gi) receptors is localized to neocortical VIP interneurons. Scale bars: 100µm (top) and 500µm (bottom). (**C**) DCZ application reduces responses in VIP interneurons (n=10 cells; N=3 mice). (**D**) In the presence of DCZ, RWS stimulation suppresses L2/3 pyramidal cell potentiation, and even causes depression, even when the CF is not co-activated (n=189 cells; N=3 mice). Left: averaged traces; middle: analysis by cell (mean ± SEM); right: response range by cell (range; box: 25th and 75th percentiles; line: median). (**E**) Circuit diagram highlighting the chemogenetic activation of VIP interneurons and recording configuration. (**F**) Expression of activating hM3D(Gq) receptors is localized to neocortical VIP interneurons. Scale bars as in (**B**). (**G**) DCZ application enhances responses in VIP interneurons (n=14 cells; N=3 mice). (**H**) In the presence of DCZ, pyramidal cell potentiation is observed, despite of CF co-activation (n=202 cells; N=4 mice). Data analysis as presented in (**D**). Scale bars: 0.1 ΔF/F; 0.5s.

Fig. 5. A pathway from the cerebellar nuclei via the zona incerta and thalamic nucleus POm to S1 cortex. (**A**) Schematic of dual-injection strategy to label outputs of zona incerta (ZI) neurons receiving input from contralateral cerebellar nuclei. Scale bar: 1mm. (**B**) EYFP expression in ZI (left) with a higher-magnification image (same slice). Right: labeled axons in the posterior medial nucleus (POm; bottom; scale bar: 20μm) and S1 cortex (top; scale bar: 10μm). (**C**) Distribution of projections from cerebellar nuclei to the ZI along the rostro-caudal axis; dotted line separates ventral (vZI) and dorsal ZI (dZI). Scale bars: 500μm. (**D**) Labeling strategy for recordings shown in (**E**). Scale bar: 1mm. (**E**) Top: Whole-cell patch-clamp recordings from POm-projecting ZI neurons receiving innervation from cerebellar nuclei. Responses to depolarizing current pulses in the absence (left) and presence (right) of TTX (1μM). Bottom: Responses to photostimulation of ChR2-expressing terminals from cerebellar nuclei neurons. (**F**) Amplitude (left) of photostimulation-evoked EPSPs and latency (right) in control recordings (n=5) and after wash-in of TTX (n=3). (**G**) Experimental configuration for recordings from mice expressing inhibiting hM4D(Gi) receptors in PV-expressing ZI interneurons. (**H**) In the presence of DCZ, the suppressive effect of CF co-activation on basic whisker responses in L2/3 pyramidal neurons is blocked (n=80 cells; N=3 mice). (**I**) Bar graphs: analysis by neuron. Data: mean ± SEM.

Fig. S1. Optogenetic CF activation causes GCaMP6f-encoded calcium transients in Purkinje cells. (**A**) Schematic of IO injection. Top left: Cerebellum (calbindin-staining of PCs) and IO (as in Fig 1B). Bottom: ChR2 expression in the IO proper (IOPr) and dorsal IO (IOD). Scale bars: 1mm (top) and 100µm (bottom). (**B**) Overlap of VGluT2-stained CF terminals with ChR2 expression in the contralateral cerebellar cortex. Scale bar: 40µm. (**C**) Post-hoc verification of ChR2 expression in CF terminals in crus I and II. Scale bars: 50µm. (**D**) Measure of distance of the pial surface to the cerebellar nuclei. While the IO innervates both the cerebellar cortex and nuclei directly, it is unlikely that CF terminals other than the superficial ones innervating PCs are optogenetically activated as the intensity of blue light decreases exponentially in brain tissue. Scale bar: 300µm. Dashed line: 2mm. (**E**) Experimental schematic for (**F** – **H**). (**F**) Calcium transients evoked by 470nm, 50ms LED light pulses in PCs in crus I/II (n=131 cells; N=2 mice) in comparison to spontaneous events (left). Scale bars: 0.1 $\Delta F/F$; 0.5s. Test of various stimulus protocols: 3x15ms, 2x20ms, 1x50ms (interval 50ms) and (3x15ms)*2 (interval 50ms). (**G**) Traces show response averages (n=102 cells from one mouse). (**H**) Bar graphs showing response peaks (left) and integrals (right). Data: mean ± SEM.

Fig. S2. Plasticity in different types of neurons. (**A**) Experimental schematic. (**B**) Event probability around stimulus onset with the window for detection of stimulus-evoked events (red; three standard deviations above the mean event probability, calculated across all frames collected during the 20-second trial periods). (**C**) Pie chart indicating the percentage of L2/3 pyramidal cells recruited or suppressed by RWS/RWS+CF activity (only responsive to whisker stimulation in post- or pre- periods, respectively) and how many remained entirely unresponsive. (**D**) Left: RWS-evoked response changes in L2/3 pyramidal neurons (n=318 cells; N=10 mice). Right: RWS+CF-evoked response changes in L2/3 pyramidal neurons (n=597 cells; N=11 mice). Bar graphs quantify calcium responses across all cells and trials, including unresponsive neurons and those not meeting evoked event criteria. (**E**) Data in (**D**) binned across time, demonstrating the tine course of RWS- and RWS+CF-induced response changes. (**F**+**G**) The same as (**D**+**E**) in INs in the same mice (n=590 cells for RWS; n=590 cells for RWS+CF). (**H**+**I**) Same as (**D**+**E**) in tdTomato-tagged interneurons that directly target pyramidal cells (PV/SST interneurons; n=106 cells, N=8 mice for RWS; n=144 cells, N=7 mice for RWS+CF). Scale bars: 0.1 ΔF/F; 0.5s. Data: mean ± SEM.

Fig. S3. Impact of RWS- and RWS+CF-stimulation on animal motion. (**A**) Experimental schematic. Mice are awake and head-fixed but can walk/run on the treadmill. (**B**) Average cross-correlation coefficient between neural calcium signals and movement activity data, segregated by neuron type. The numbers below the box charts indicate the number of recorded cells. (**C**) Left: probability distribution of animal movement in Rest trials, demonstrating the absence of movement both before and after stimulus onset. Right: probability distribution of animal movement in Active trials. (**D**) Pie charts indicating the percentage of rest, active and stop trials pre-vs post-RWS (left) or RWS+CF (right). (**E**) Average probability of animal movement in Rest trials pre- and post-RWS (left) or RWS+CF (right) over the same time scale as the neural traces shown below. (**F**) and (**H**) RWS-evoked potentiation in L2/3 pyramidal neurons (n=124; N=10) and RWS+CF-mediated suppression of potentiation (n=388; N=11) in the absence of animal movement (i.e. in Rest trials). (**G**) and (**I**) Analysis for INs in the same mice. Scale bars: 0.1 $\Delta F/F$; 0.5s. Data: mean ± SEM. Note that motion activity traces capture both whisking and running activity.

Fig. S4. Intrinsic optical imaging confirms CF-mediated suppression of S1 plasticity. (**A**) Experimental schematic. Intrinsic optical imaging is performed using a high-speed camera. The field of view is illuminated with red light (625 nm). A decrease in reflectance indicates increased oxygen consumption by neurons activated by single whisker stimulation (blue arrow). (**B**) Top: Example of S1 plasticity evoked by stimulation of the C2 whisker at 10Hz. Bottom: Example of suppression of response potentiation when whisker stimulation is paired with optogenetic CF co-activation at 1Hz. (**C**) Quantification of RWS-evoked potentiation of the single whisker response area (blue; N=4 mice) and RWS+CF-mediated suppression of response potentiation (red; N=4 mice). No response potentiation is observed in the absence of repeated whisker stimulation or CF activation (grey; N=4 mice). Data are normalized to the baseline response area. Light blue line indicates mean.

Fig. S5. Chemogenetic manipulation of interneuron activity: plasticity effects in L2/3 pyramidal cells vs control. (**A**) Chemogenetic activation of SST interneurons. Left: Experimental schematic. Middle: circuit diagram. Right: DCZ injection activates SST interneurons (green). Top: Control protocol. 'Post' marks the period equivalent in time to the period for the measurement of plasticity effects after RWS (bottom). (**B**) Response amplitudes in L2/3 pyramidal neurons during Pre, DCZ wash-in, and Post periods in control experiments. (**C**) Responses in L2/3 pyramidal cells to whisker stimulation in the Post period relative to the responses in the DCZ wash-in period (control: n=218 cells; N=3 mice; plasticity: n=253 cells; N=4 mice; data in control and plasticity experiments are normalized to the control experiment). (**D**) – (**F**) Equivalent measures during chemogenetic VIP interneuron inhibition (red; control: n=173 cells; N=3 mice; plasticity: n=164 cells; N=3 mice). (**G**) – (**I**) Equivalent measures during chemogenetic SST interneuron inhibition (control: n=175 cells; N= 3 mice; plasticity: n=181 cells; N=3 mice). (**J**) – (**L**) Equivalent measures during chemogenetic VIP interneuron activation (control: 145 cells; N=3 mice; plasticity: n=197 cells; N=4 mice). Optogenetic CF co-activation is applied during RWS in the experiments shown in (**G**) – (**L**). Data: mean ± SEM. Note that in all experiments but the chemogenetic VIP inhibition the plasticity effect can be separated from the chemogenetic manipulation itself.

Fig. S6. Transsynaptic labeling identifies projections from the cerebellar nuclei to POm. (**A**) Schematic of dual-injection approach to label outputs of zona incerta (ZI) neurons receiving input from the contralateral cerebellar nuclei. (**B**) Fibers from the contralateral cerebellar nuclei reach the zona incerta (ZI; within dashed lines) and project out of the ZI (top right; arrowheads). Scale bar: 100µm. (**C**) These fibers reach thalamic nucleus POm (arrowheads). Scale bar: 50µm. (**D**) and (**E**) Zoomed-out projections showing the spatial relationship of ZI and POm (**D**) and fiber projections in POm (**E**). Scale bars: D (left): 1mm; D (right): 500µm; E: 200µm. (**F**) Series of coronal sections along the rostro-caudal axis showing details of the projections from the contralateral cerebellar nuclei to ZI and POm. Scale bars: 1mm. POt = posterior thalamic nucleus (triangular part). Colored dots mark identical sections.

Fig. S7. Cerebellar nuclei do not strongly project to thalamic reticular nucleus. (**A**) Schematic of labeling approach (top) and injection site of retrograde tracer (bottom). Scale bar: 1mm. (**B**) Image of retrograde label from the somatosensory thalamus (POm and VPm; cyan) and orthograde label from the contralateral cerebellar nuclei (red) taken approximately -1.0mm posterior from bregma, demonstrating lack of overlap between neurons in the thalamic reticular nucleus (TRN) and cerebellar nuclei terminals in the adjacent thalamic nuclei. Representative images are shown from two separate mice. Scale bars: 1mm (left images) and 250µm (right images). (**C**) Projection diagram. DCN: deep cerebellar nuclei; ZI: zona incerta; POm: posterior medial thalamic nucleus; TRN: thalamic reticular nucleus; VPm: ventral posterior medial nucleus; VPL: ventral posterior lateral nucleus; VA: ventral anterior nucleus; VL: ventral lateral nucleus.

Fig. S8. Whole-cell patch-clamp recordings are performed from neurons in the ZI that project to POm and receive input from cerebellar nuclei. (**A**) Left: Differential interference contrast (DIC) image showing the ZI (white dashed circle) at low magnification (top; scale bar: 500μm), and a neuron selected for patching at higher magnification (bottom; scale bar: 100μm). Middle left: same images showing ChR2-expression. Middle right: same images showing retrograde fluororuby label originating in the POm. Right: merged images (boxed area with yellow dashed line marks the recordings area shown in the images below). (**B**) Post-hoc histology of an acute slice used for recordings demonstrating the details of cerebellar innervation of the ZI, separated by dorsal ZI (dZI) and ventral ZI (vZI; image corresponds to Fig. 5D, separated by channel). Scale bar: 500μm. (**C**) Quantification of the terminal fluorescence segregated by dZI and vZI. Data: mean ± SEM.

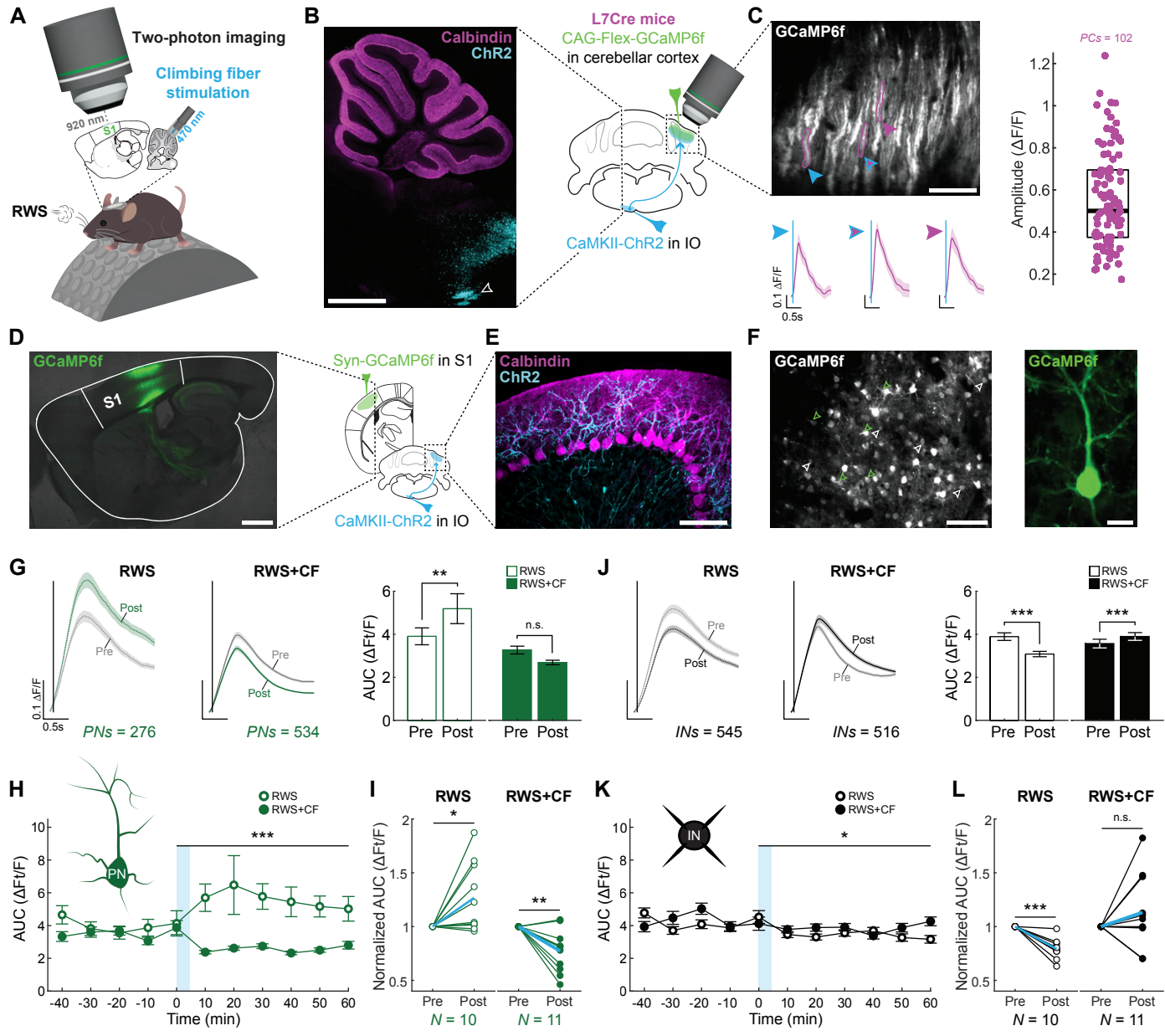

A
Two-photon imaging
Climbing fiber stimulation
920 nm
S1
470 nm
RWS
B
Calbindin
ChR2
L7Cre mice
CAG-Flex-GCaMP6f
in cerebellar cortex
CaMKII-ChR2 in IO
C
GCaMP6f
0.1 ΔF/F
0.5s
PCs = 102
Amplitude (ΔF/F)
D
GCaMP6f
S1
Syn-GCaMP6f in S1
CaMKII-ChR2 in IO
E
Calbindin
ChR2
F
GCaMP6f
GCaMP6f
G
RWS
RWS+CF
Post
Pre
0.1 ΔF/F
0.5s
PNs = 276
PNs = 534
AUC (ΔFt/F)
RWS
RWS+CF
**
n.s.
Pre
Post
J
RWS
RWS+CF
Pre
Post
INs = 545
INs = 516
***
H
RWS
RWS+CF
PN
***
AUC (ΔFt/F)
Time (min)
I
RWS
RWS+CF
*
**
Normalized AUC (ΔFt/F)
N = 10
N = 11
K
IN
*
L
RWS
RWS+CF
n.s.
***
N = 10
N = 11

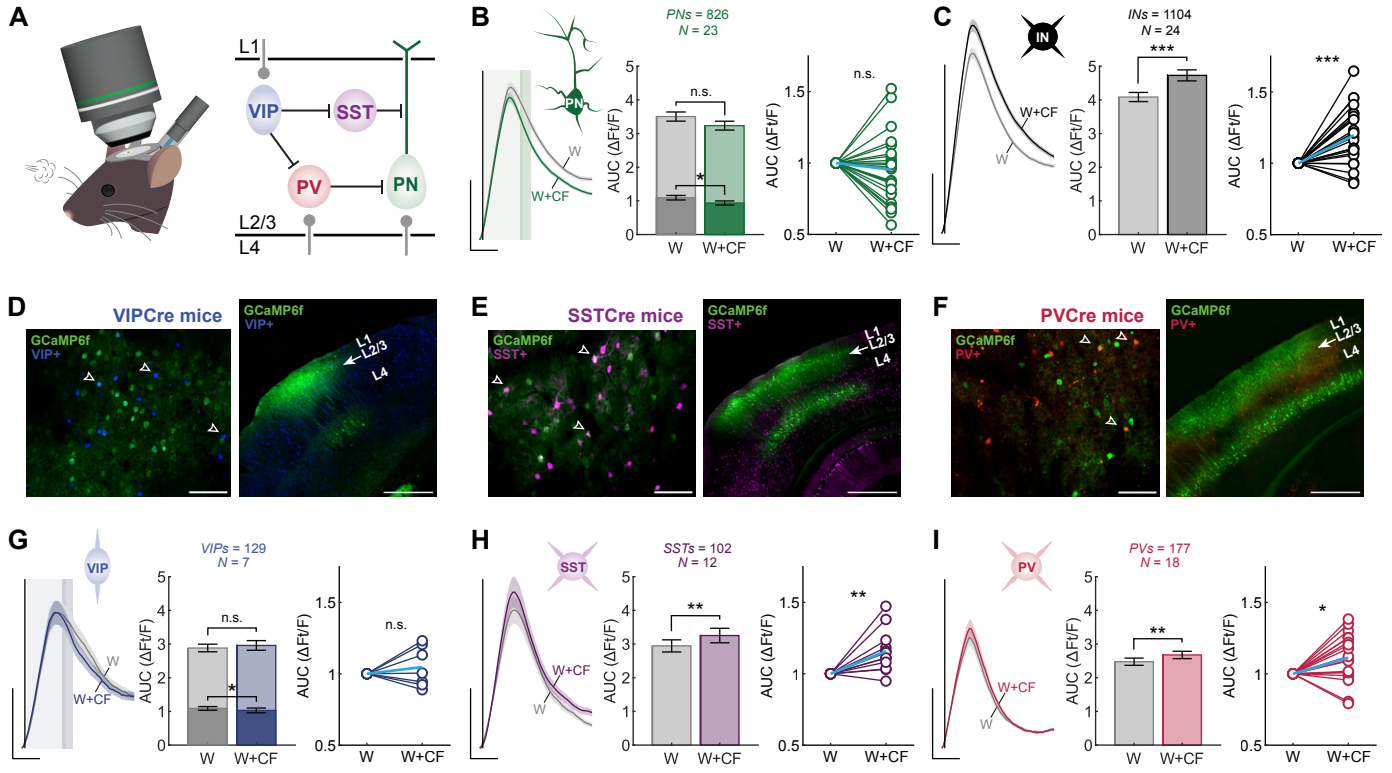
A
L1
VIP
SST
PV
PN
L2/3
L4
B
PNs = 826
N = 23
PN
W
W+CF
AUC (ΔFt/F)
n.s.
*
W
W+CF
C
IN
INs = 1104
N = 24
***
W+CF
W
D
VIPCre mice
GCaMP6f
VIP+
L1
L2/3
L4
E
SSTCre mice
SST+
F
PVCre mice
PV+
G
VIP
VIPs = 129
N = 7
H
SST
SSTs = 102
N = 12
**
I
PV
PVs = 177
N = 18

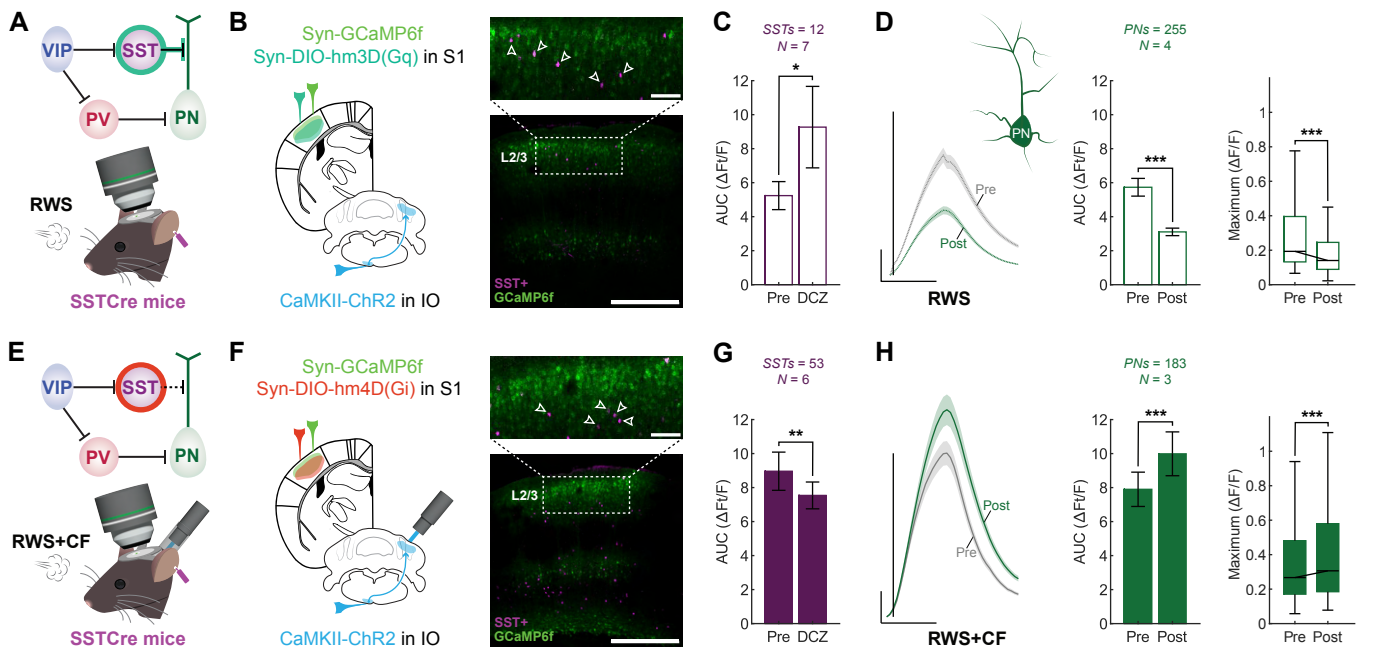
A
VIP
SST
PV
PN
RWS
SSTCre mice
B
Syn-GCaMP6f
Syn-DIO-hm3D(Gq) in S1
CaMKII-ChR2 in IO
L2/3
SST+
GCaMP6f
C
SSTs = 12
N = 7
AUC (ΔFt/F)
Pre
DCZ
D
PN
Pre
Post
RWS
PNs = 255
N = 4
AUC (ΔFt/F)
Maximum (ΔF/F)
E
VIP
SST
PV
PN
RWS+CF
SSTCre mice
F
Syn-GCaMP6f
Syn-DIO-hm4D(Gi) in S1
CaMKII-ChR2 in IO
L2/3
SST+
GCaMP6f
G
SSTs = 53
N = 6
AUC (ΔFt/F)
Pre
DCZ
H
Post
Pre
RWS+CF
PNs = 183
N = 3
AUC (ΔFt/F)
Maximum (ΔF/F)

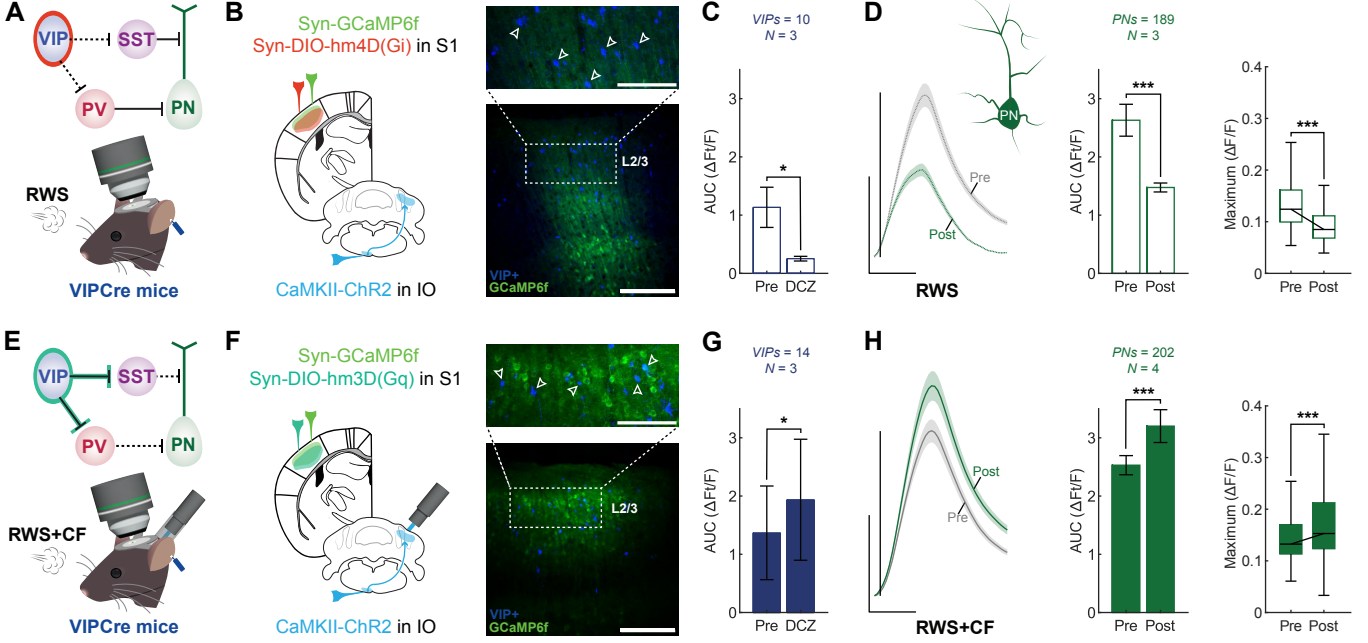
A
VIP
SST
PV
PN
RWS
VIPCre mice
B
Syn-GCaMP6f
Syn-DIO-hm4D(Gi) in S1
CaMKII-ChR2 in IO
L2/3
VIP+
GCaMP6f
C
VIPs = 10
N = 3
AUC (ΔFt/F)
Pre DCZ
D
PN
Pre
Post
RWS
PNs = 189
N = 3
Maximum (ΔF/F)
Pre Post
E
RWS+CF
VIPCre mice
F
Syn-GCaMP6f
Syn-DIO-hm3D(Gq) in S1
CaMKII-ChR2 in IO
G
VIPs = 14
N = 3
H
RWS+CF
PNs = 202
N = 4

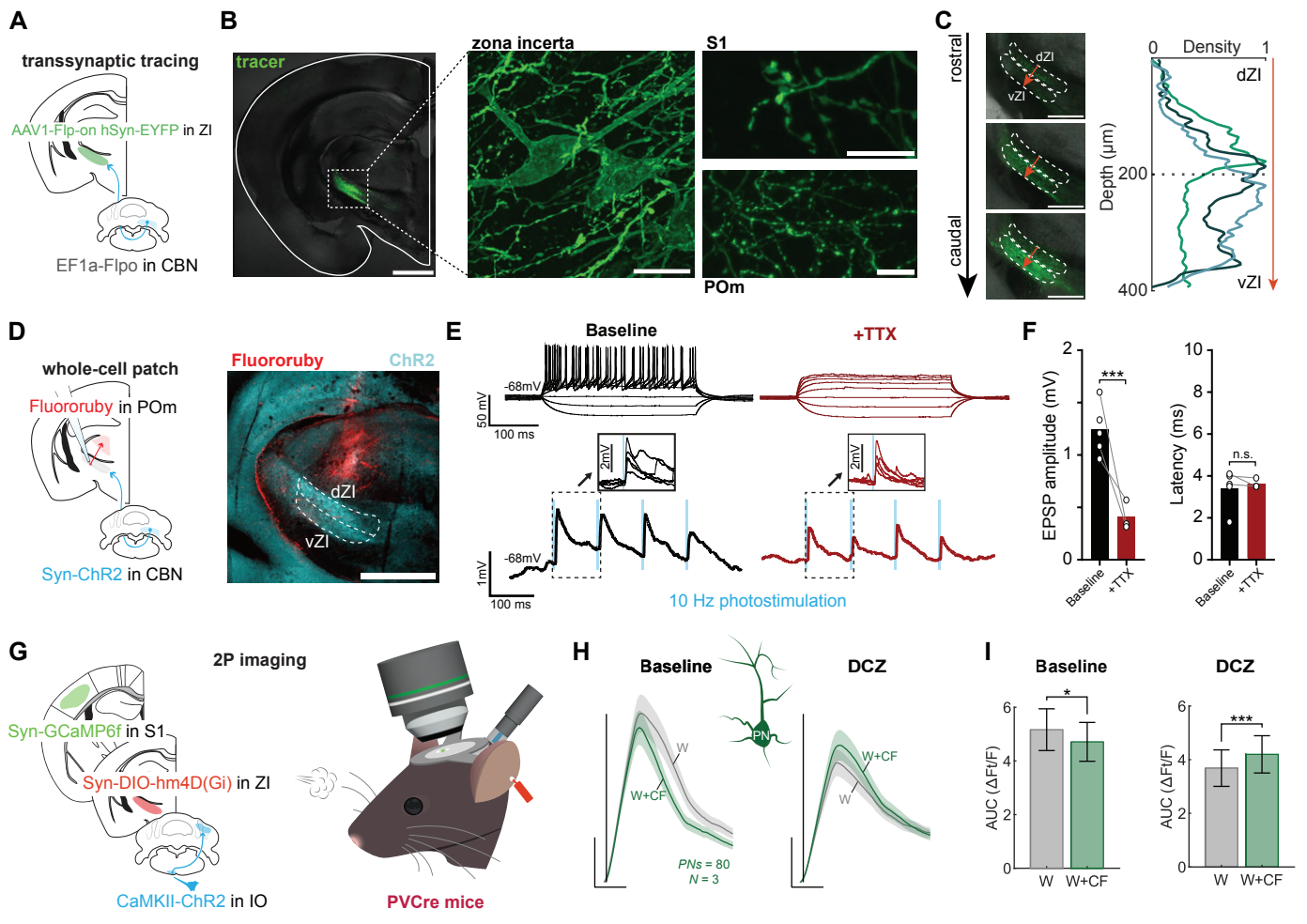
A
transsynaptic tracing
AAV1-Flp-on hSyn-EYFP in ZI
EF1a-Flpo in CBN
B
tracer
zona incerta
S1
POm
C
rostral
caudal
dZI
vZI
Depth (μm)
Density
0
1
200
400
D
whole-cell patch
Fluororuby in POm
Syn-ChR2 in CBN
Fluororuby
ChR2
dZI
vZI
E
Baseline
+TTX
-68mV
50 mV
100 ms
2mV
1mV
10 Hz photostimulation
F
EPSP amplitude (mV)
Latency (ms)
***
n.s.
Baseline
+TTX
G
2P imaging
Syn-GCaMP6f in S1
Syn-DIO-hm4D(Gi) in ZI
CaMKII-ChR2 in IO
PVCre mice
H
Baseline
DCZ
PN
W
W+CF
PNs = 80
N = 3
I
Baseline
DCZ
AUC (ΔF/F)
*
***
W
W+CF

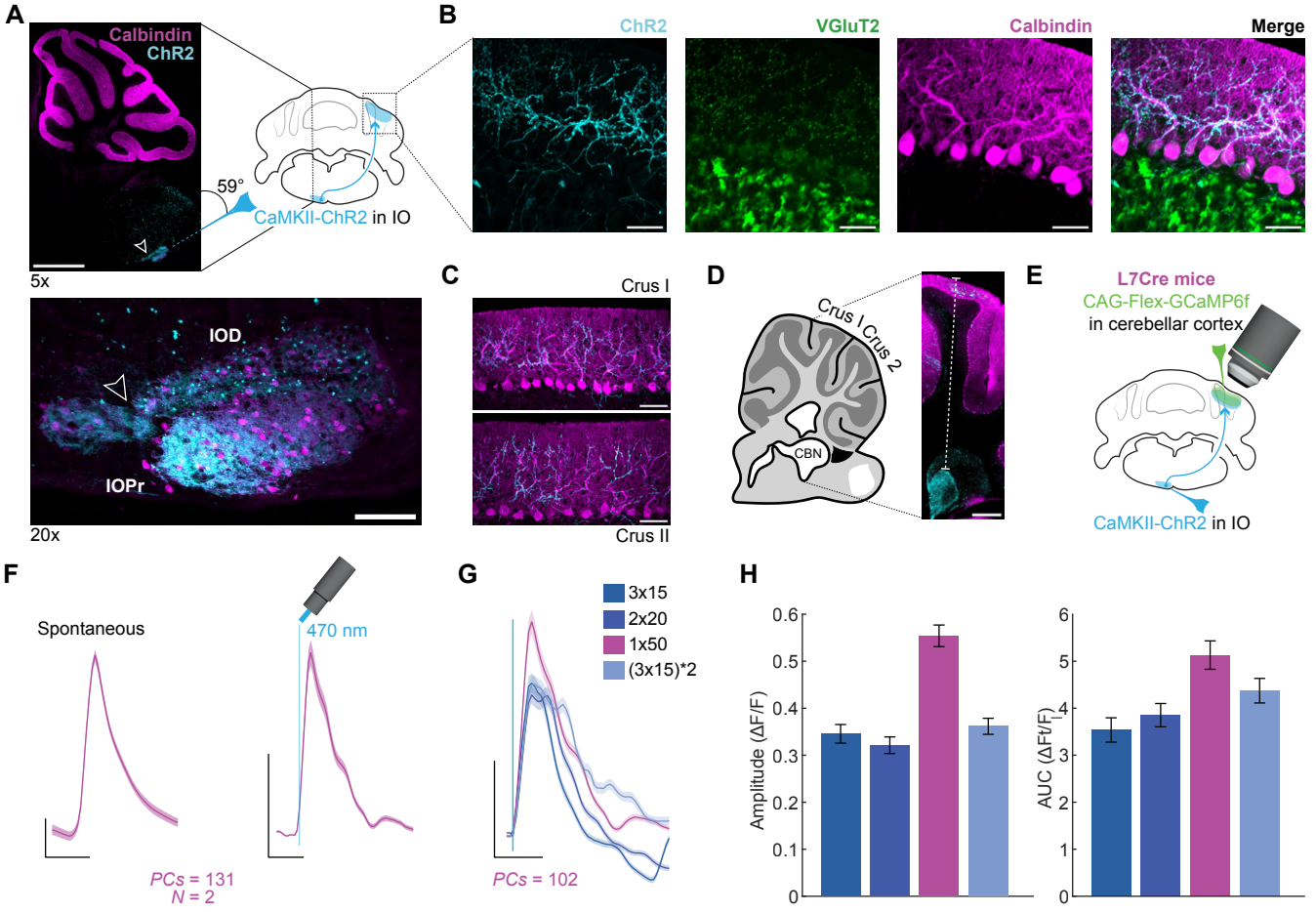
A
Calbindin
ChR2
59°
CaMKII-ChR2 in IO
5x
IOD
IOPr
20x
B
ChR2
VGluT2
Calbindin
Merge
C
Crus I
Crus II
D
Crus I
Crus 2
CBN
E
L7Cre mice
CAG-Flex-GCaMP6f
in cerebellar cortex
CaMKII-ChR2 in IO
F
Spontaneous
470 nm
PCs = 131
N = 2
G
3x15
2x20
1x50
(3x15)*2
PCs = 102
H
Amplitude (ΔF/F)
AUC (ΔF/F)

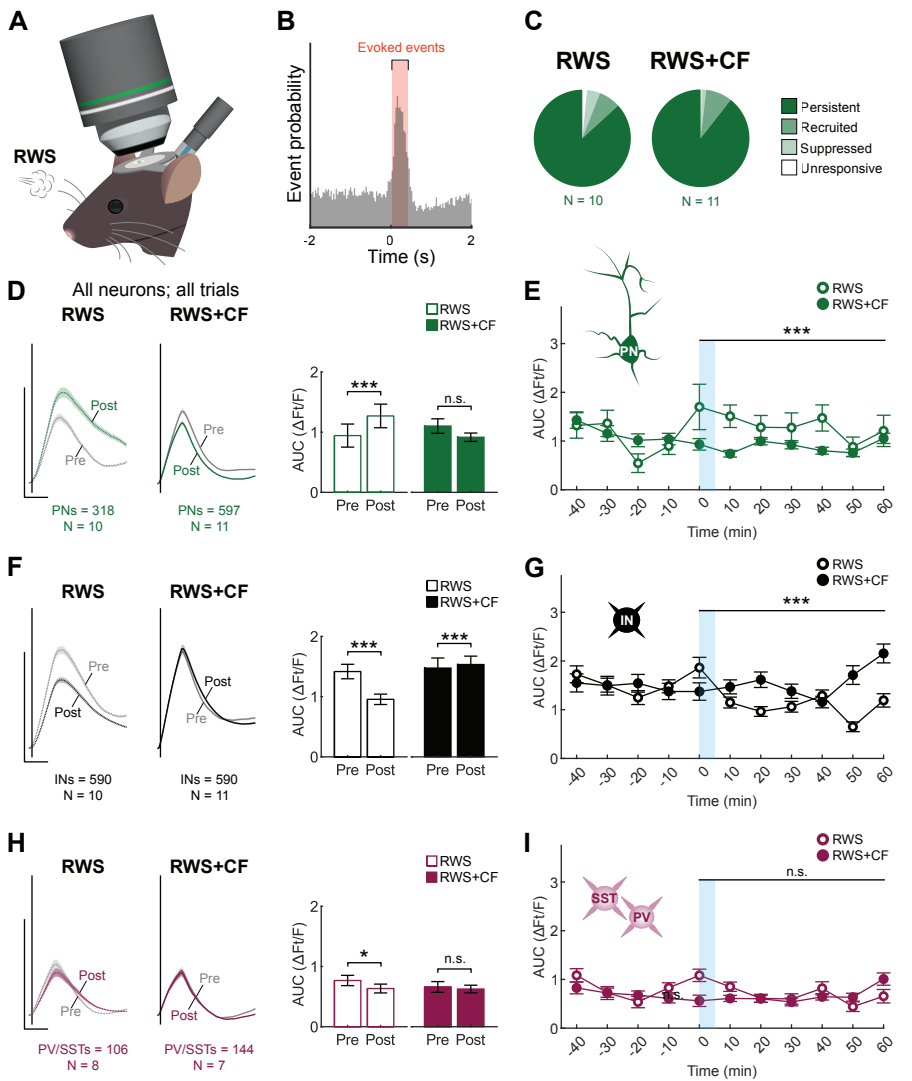
A
RWS
B
Evoked events
Event probability
-2
0
2
Time (s)
C
RWS
RWS+CF
Persistent
Recruited
Suppressed
Unresponsive
N = 10
N = 11
D
All neurons; all trials
RWS
RWS+CF
Post
Pre
PNs = 318
N = 10
PNs = 597
N = 11
RWS
RWS+CF
AUC (ΔFt/F)
***
n.s.
Pre Post
Pre Post
E
PN
RWS
RWS+CF
***
AUC (ΔFt/F)
Time (min)
F
RWS
RWS+CF
Pre
Post
INs = 590
N = 10
INs = 590
N = 11
RWS
RWS+CF
AUC (ΔFt/F)
***
***
Pre Post
Pre Post
G
IN
RWS
RWS+CF
***
AUC (ΔFt/F)
Time (min)
H
RWS
RWS+CF
Post
Pre
PV/SSTs = 106
N = 8
PV/SSTs = 144
N = 7
RWS
RWS+CF
AUC (ΔFt/F)
*
n.s.
Pre Post
Pre Post
I
SST
PV
RWS
RWS+CF
n.s.
n.s.
AUC (ΔFt/F)
Time (min)

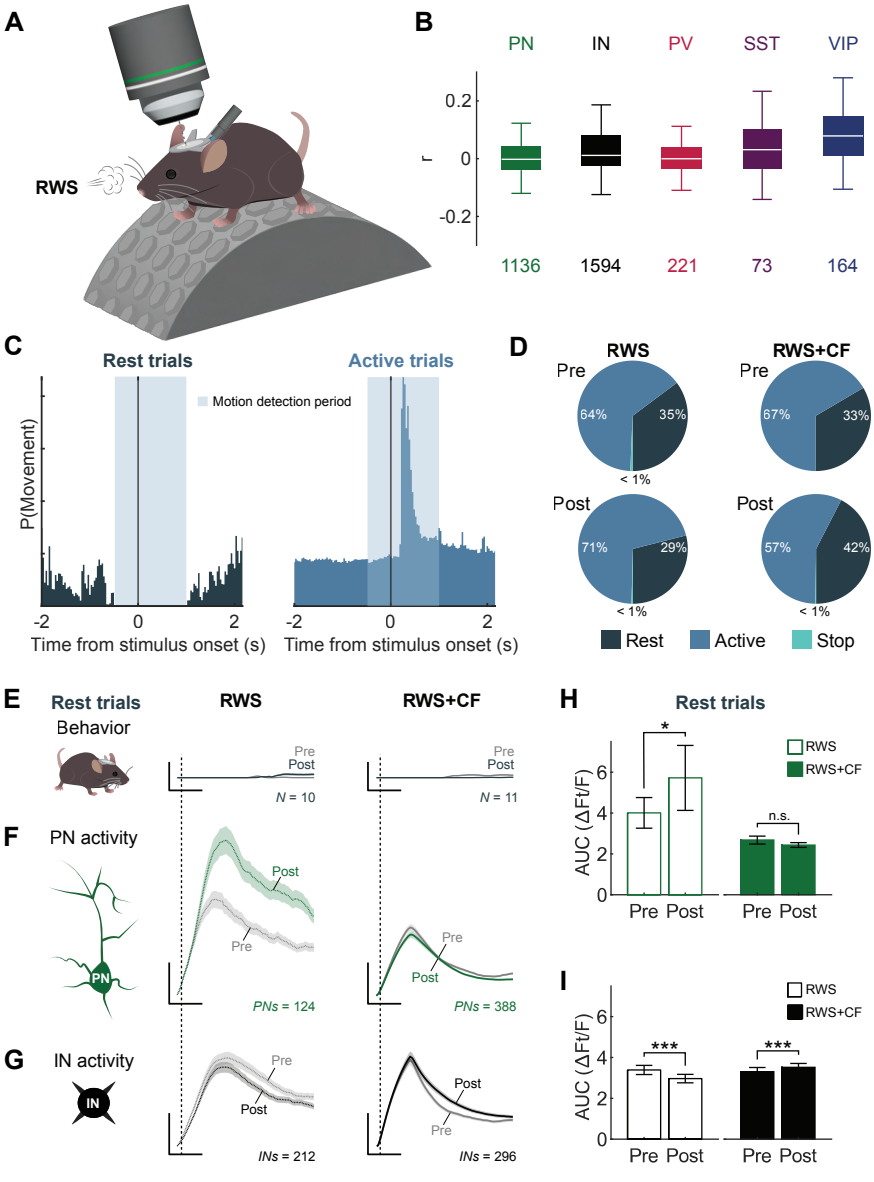
A
RWS
B
PN
IN
PV
SST
VIP
r
0.2
0
-0.2
1136
1594
221
73
164
C
Rest trials
Active trials
Motion detection period
P(Movement)
-2
0
2
Time from stimulus onset (s)
D
RWS
RWS+CF
Pre
Post
64%
35%
< 1%
67%
33%
71%
29%
57%
42%
Rest
Active
Stop
E
Rest trials
Behavior
RWS
RWS+CF
Pre
Post
N = 10
N = 11
F
PN activity
PN
PNs = 124
PNs = 388
G
IN activity
IN
INs = 212
INs = 296
H
Rest trials
AUC (ΔFt/F)
RWS
RWS+CF
*
n.s.
I
***

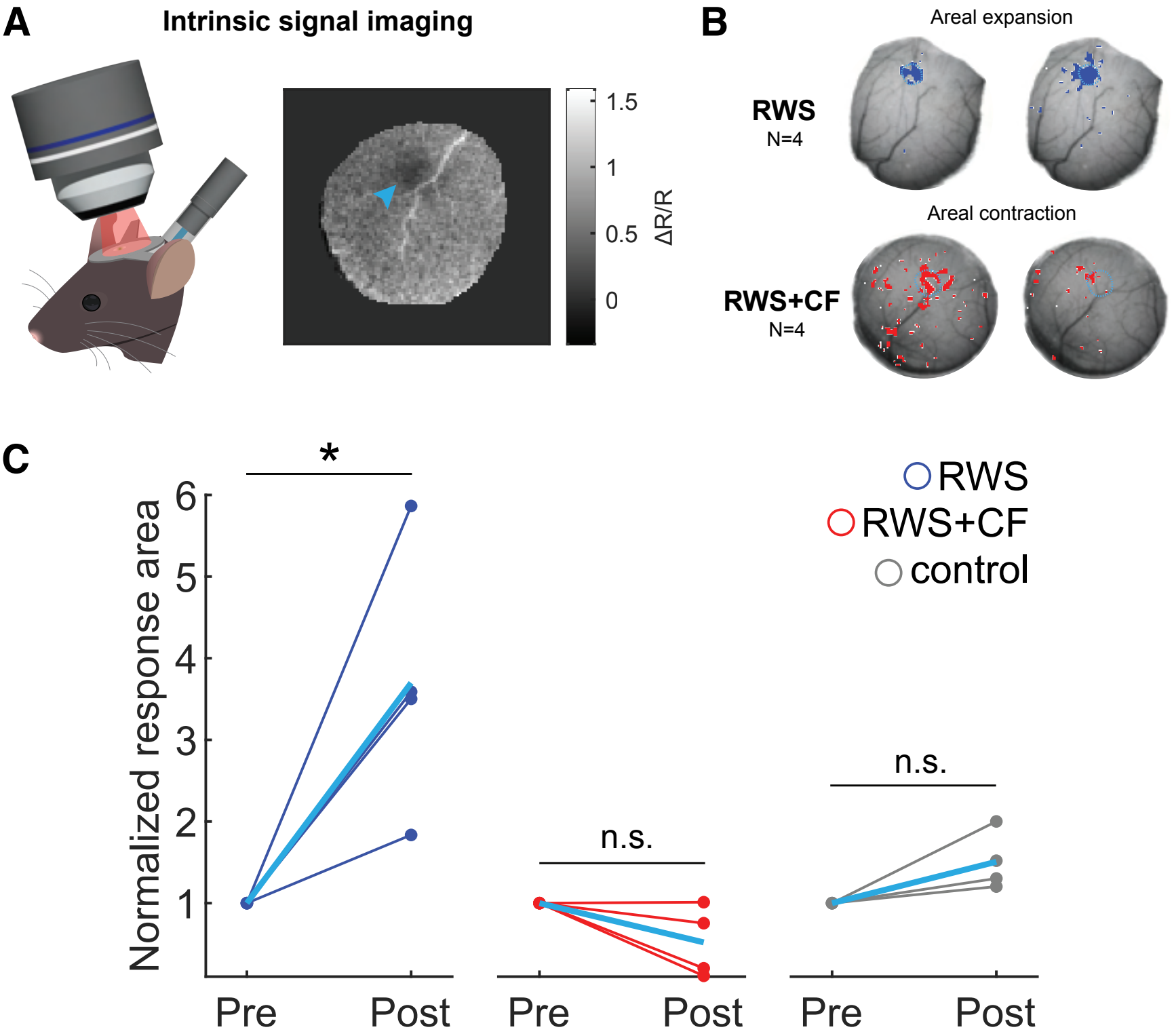
A
Intrinsic signal imaging
1.5
1
0.5
0
ΔR/R
B
Areal expansion
RWS
N=4
Areal contraction
RWS+CF
N=4
C
*
Normalized response area
6
5
4
3
2
1
Pre
Post
n.s.
Pre
Post
n.s.
Pre
Post
RWS
RWS+CF
control

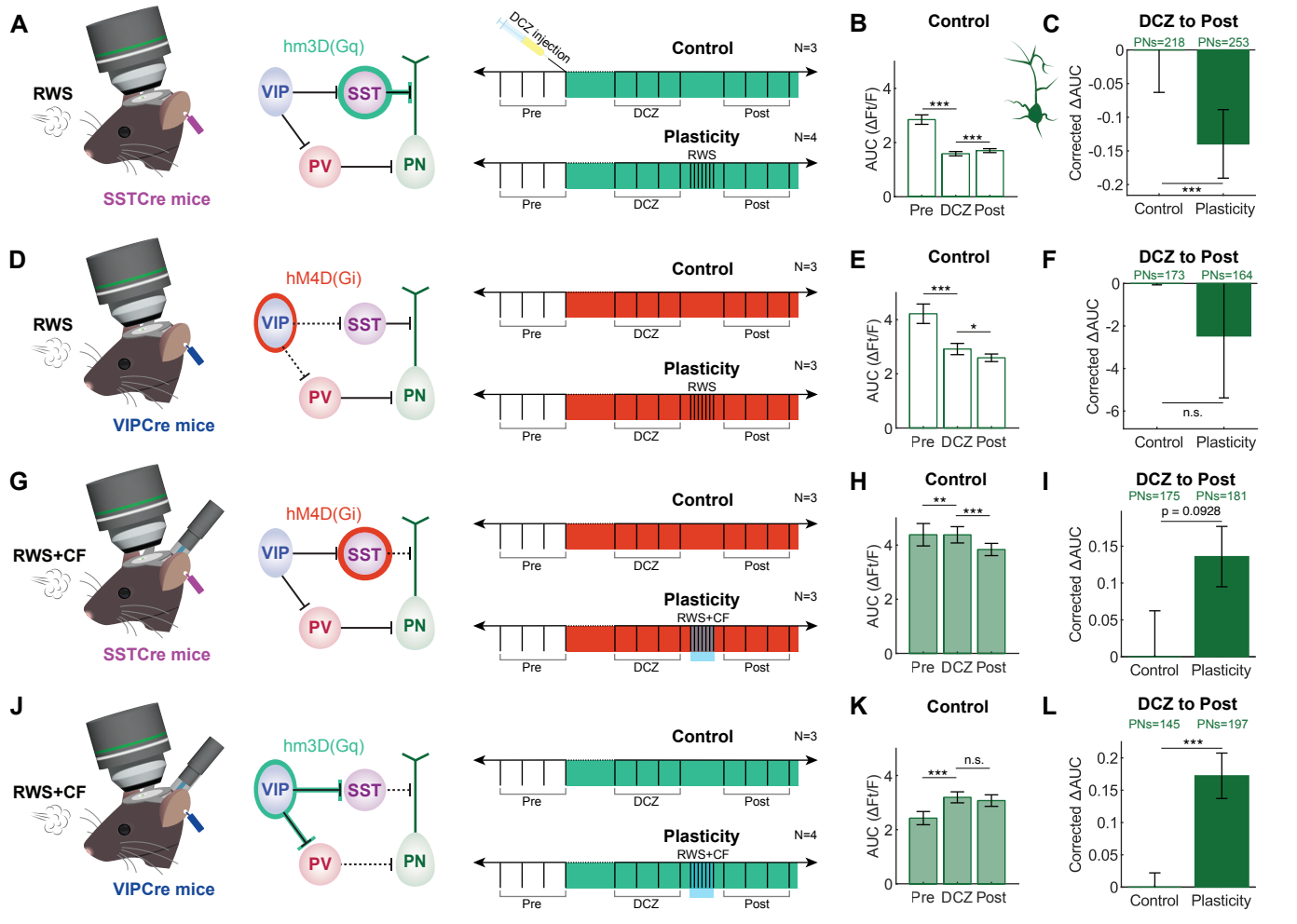
A
RWS
SSTCre mice
hm3D(Gq)
VIP
SST
PV
PN
DCZ injection
Control
N=3
Pre
DCZ
Post
Plasticity
N=4
RWS
B
Control
AUC (ΔFt/F)
Pre DCZ Post
C
DCZ to Post
PNs=218
PNs=253
Corrected ΔAUC
Control Plasticity
D
RWS
VIPCre mice
hM4D(Gi)
E
F
PNs=173
PNs=164
n.s.
G
RWS+CF
SSTCre mice
RWS+CF
H
I
PNs=175
PNs=181
p = 0.0928
J
VIPCre mice
K
L
PNs=145
PNs=197

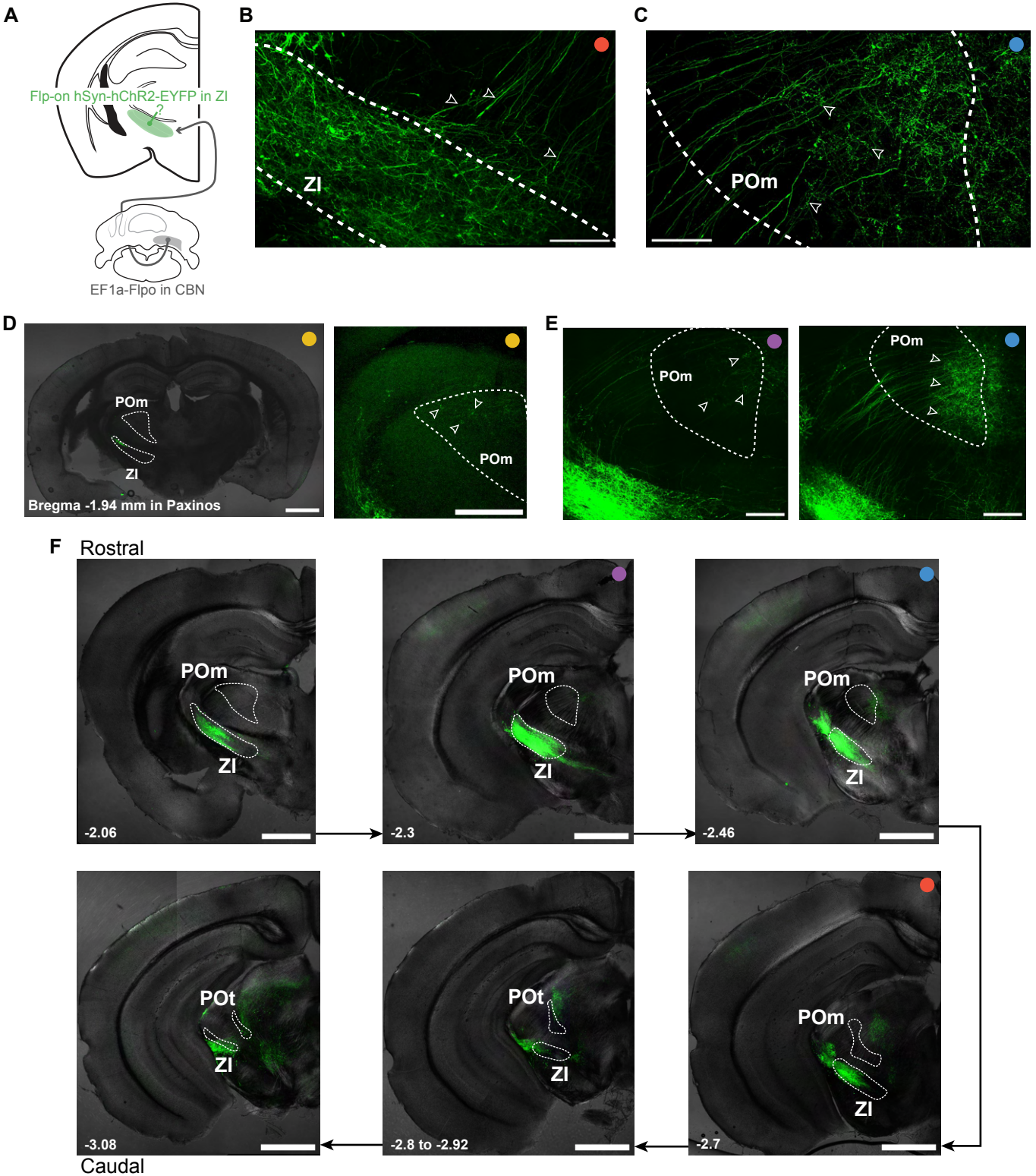
A
Flp-on hSyn-hChR2-EYFP in ZI
?
EF1a-Flpo in CBN
B
ZI
C
POm
D
POm
ZI
Bregma -1.94 mm in Paxinos
POm
E
POm
POm
F
Rostral
POm
ZI
-2.06
POm
ZI
-2.3
POm
ZI
-2.46
POt
ZI
-3.08
POt
ZI
-2.8 to -2.92
POm
ZI
-2.7
Caudal

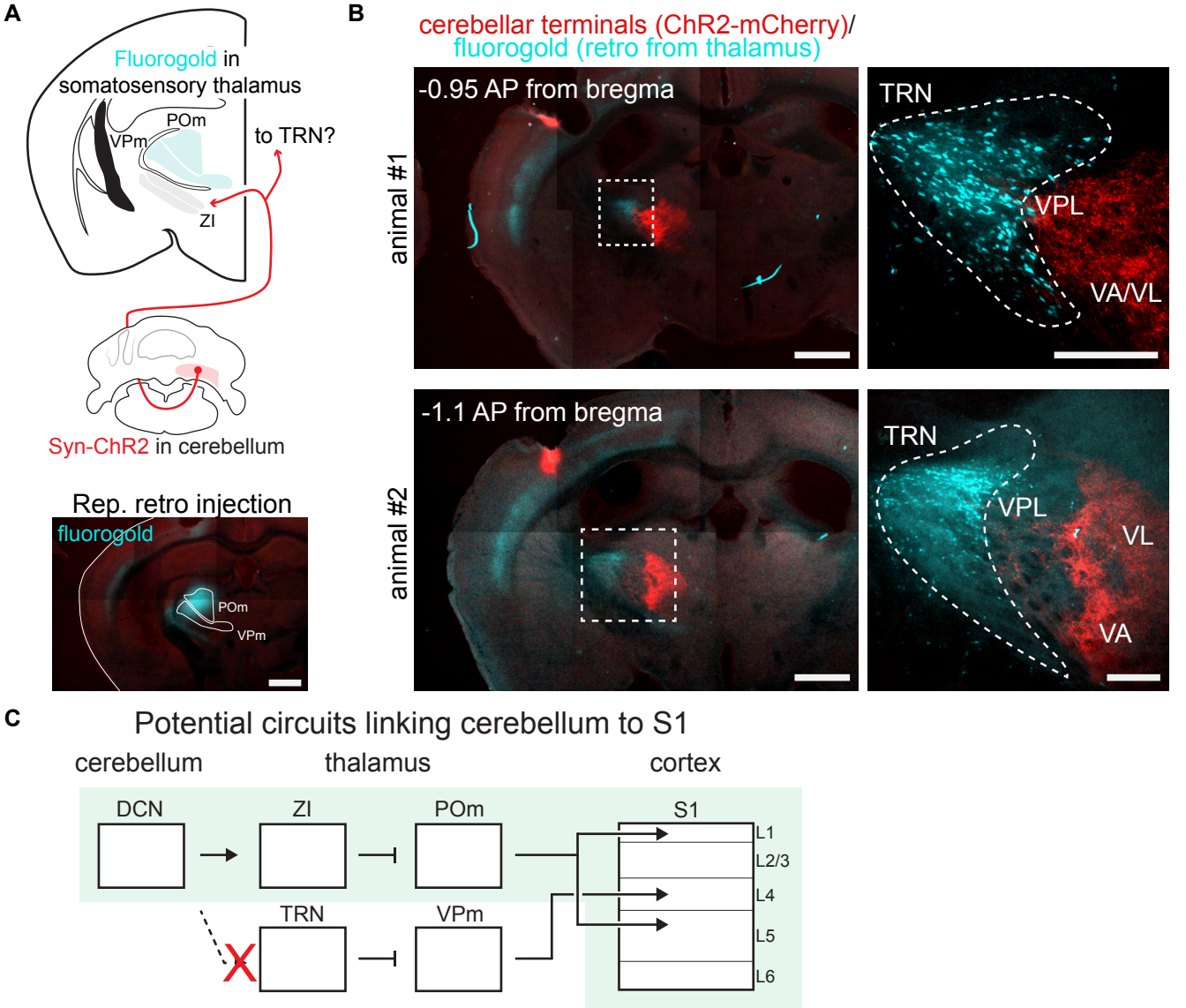
A
Fluorogold in
somatosensory thalamus
POm
VPm
to TRN?
ZI
Syn-ChR2 in cerebellum
Rep. retro injection
fluorogold
POm
VPm
B
cerebellar terminals (ChR2-mCherry)/
fluorogold (retro from thalamus)
animal #1
-0.95 AP from bregma
TRN
VPL
VA/VL
animal #2
-1.1 AP from bregma
TRN
VPL
VL
VA
C
Potential circuits linking cerebellum to S1
cerebellum
thalamus
cortex
DCN
ZI
POm
S1
L1
L2/3
L4
L5
L6
TRN
VPm

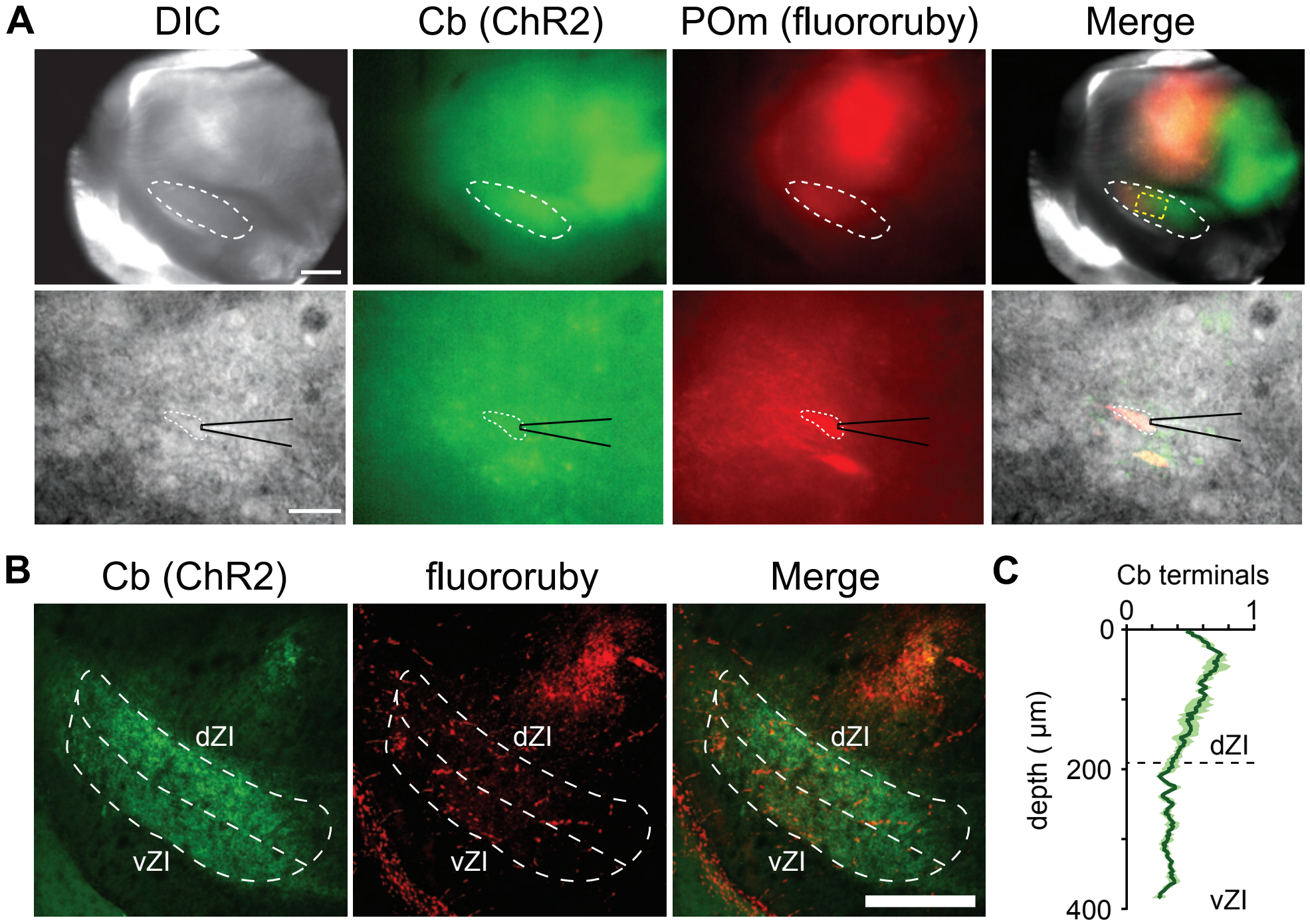
A
DIC
Cb (ChR2)
POm (fluororuby)
Merge
B
Cb (ChR2)
fluororuby
Merge
dZI
vZI
dZI
vZI
dZI
vZI
C
Cb terminals
0
1
0
200
400
depth (µm)
dZI
vZI

panel		mean	median	error	n cells	N mice	test	*P* value	result	measurement (units)	cell type
1.C		0.554	0.5004	0.023	102	1	N/A	N/A	N/A	Amplitude (ΔF/F)	PC
1.G	Pre (RWS)	3.9059	2.3829	0.3925	276†	10	Wilcoxon	0.0011	**	AUC ((ΔF*t)/F)	PN
	Post (RWS)	5.1908	2.4519	0.6948							
	Pre (RWS+CF)	3.2676	1.9988	0.1811	534†	11	Wilcoxon	0.1126	n.s.		
	Post (RWS+CF)	2.6892	2.0035	0.1049							
1.H	-40 min (RWS)	4.65494	N/A	0.5576	134†	8	Two-way ANOVA	<0.001	***	AUC ((ΔF*t)/F)	PN
	-30 min (RWS)	3.81658		0.4105	164†	9					
	-20 min (RWS)	3.55023		0.379	161†	9					
	-10 min (RWS)	3.86943		0.511	202†	10					
	0 min (RWS)‡	4.13362		0.7696	95†	6					
	10 min (RWS)‡	5.69981		0.8354	205†	10					
	20 min (RWS)‡	6.47522		1.7941	206†	10					
	30 min (RWS)‡	5.77442		0.7801	146†	8					
	40 min (RWS)‡	5.44768		0.9046	150†	8					
	50 min (RWS)‡	5.16559		0.6383	111†	8					
	60 min (RWS)‡	5.02273		0.7503	54†	4					
	- 40 min (RWS+CF)	3.32904		3.329	351†	10					
	-30 min (RWS+CF)	3.60127		3.6013	317†	10					
	- 20 min (RWS+CF)	3.69046		3.6905	364†	10					
	-10 min (RWS+CF)	3.05876		3.0588	394†	11					
	0 min (RWS+CF)‡	3.87257		3.8726	204†	9					
	10 min (RWS+CF)‡	2.37707		2.3771	479†	11					
	20 min (RWS+CF)‡	2.61932		2.6193	511†	11					
	30 min (RWS+CF)‡	2.74055		2.7406	483†	10					
	40 min (RWS+CF)‡	2.32432		2.3243	477†	10					
	50 min (RWS+CF)‡	2.49962		2.4996	362†	6					
	60 min (RWS+CF)‡	2.80165		2.8017	352†	4					
1.I	Pre (RWS)	1	N/A	0	276	10†	One-sample t-test	0.0282	*	AUC ((ΔF*t)/F)	PN
	Post (RWS)	1.2675		0.1024							
	Pre (RWS+CF)	1		0	534	11†	One-sample t-test	0.003	**		
	Post (RWS+CF)	0.7723		0.0584							
1.J	Pre (RWS)	3.8912	2.739	0.1763	545†	10	Wilcoxon	<0.001	***	AUC ((ΔF*t)/F)	IN
	Post (RWS)	3.0817	2.2498	0.1241							
	Pre (RWS+CF)	3.5683	2.3499	0.2021	516†	11	Wilcoxon	<0.001	***		
	Post (RWS+CF)	3.8983	2.5878	0.1797							
1.K	-40 min (RWS)	4.77216	N/A	0.303	321†	8	Two-way ANOVA	0.0183	*	AUC ((ΔF*t)/F)	IN
	-30 min (RWS)	3.70043		0.2334	357†	9					
	-20 min (RWS)	4.08059		0.2662	303†	9					
	-10 min (RWS)	3.85716		0.2184	425†	10					
	0 min (RWS)‡	4.52014		0.3909	206†	6					
	10 min (RWS)‡	3.45404		0.1886	416†	10					
	20 min (RWS)‡	3.29834		0.1827	411†	10					
	30 min (RWS)‡	3.54832		0.1943	291†	8					
	40 min (RWS)‡	3.69138		0.1958	324†	8					
	50 min (RWS)‡	3.26671		0.2273	236†	8					
	60 min (RWS)‡	3.16086		0.2327	147†	4					
	- 40 min (RWS+CF)	3.93255		0.3137	320†	10					
	-30 min (RWS+CF)	4.4692		0.396	283†	11					
	- 20 min (RWS+CF)	5.02758		0.3417	344†	10					
	-10 min (RWS+CF)	3.95778		0.278	376†	11					
	0 min (RWS+CF)‡	4.11703		0.4043	219†	10					
	10 min (RWS+CF)‡	3.7648		0.2121	444†	11					
	20 min (RWS+CF)‡	3.87636		0.2234	479†	11					
	30 min (RWS+CF)‡	3.90208		0.2237	423†	10					
	40 min (RWS+CF)‡	3.37561		0.1953	405†	10					
	50 min (RWS+CF)‡	3.8697		0.2619	314†	6					
	60 min (RWS+CF)‡	4.25666		0.2688	273†	4					
1.L	Pre (RWS)	1	N/A	0	545	10†	One-sample t-test	<0.001	***	AUC ((ΔF*t)/F)	IN
	Post (RWS)	0.7916		0.0295							
	Pre (RWS+CF)	1		0	516	11†	One-sample t-test	0.2233	n.s.		
	Post (RWS+CF)	1.1321		0.1018							

† indicates whether statistics performed across cells or mice

‡ time points included in ANOVA

panel		mean	median	error	n cells	N mice	test	*P* value	result	measurement (units)	cell type
2.B (c)	W (0-700ms)	3.5038	2.3648	0.1358	826†	23	Wilcoxon	0.1856	n.s.	AUC ((ΔF*t)/F)	PN
	W+CF (0-700ms)	3.2344	2.2292	0.1314							
	W (650-850ms)	1.0935	0.4922	0.0672			Wilcoxon	0.0487	*		
	W+CF (650-850ms)	0.937	0.4763	0.0611							
2.B (r)	W	1	N/A	0	826	23†	One-sample t-	0.3709	n.s.	AUC ((ΔF*t)/F)	PN
	W+CF	0.954		0.0504			test				
2.C (c)	W	4.0841	2.8209	0.1357	1104†	24	Wilcoxon	<0.001	***	AUC ((ΔF*t)/F)	IN
	W+CF	4.7268	3.1189	0.1637							
2.C (r)	W	1	N/A	0	1104	24†	One-sample t-	<0.001	***	AUC ((ΔF*t)/F)	IN
	W+CF	1.1961		0.0406			test				
2.G (c)	W (0-700ms)	2.883	2.529	0.1128	129†	7	Wilcoxon	0.8665	n.s.	AUC ((ΔF*t)/F)	VIP
	W+CF (0-700ms)	2.9589	2.5207	0.1438							
	W (650-850ms)	1.0888	0.9519	0.0545			Wilcoxon	0.0255	*		
	W+CF (650-850ms)	1.0294	0.8138	0.0713							
2.G (r)	W	1	N/A	0	129	7†	One-sample t-	0.4113	n.s.	AUC ((ΔF*t)/F)	VIP
	W+CF	1.047		0.0533			test				
2.H (c)	W	2.9453	2.3916	0.18	102†	12	Wilcoxon	0.001	**	AUC ((ΔF*t)/F)	SST
	W+CF	3.2532	2.7647	0.2152							
2.H (r)	W	1	N/A	0	102	12†	One-sample t-	0.0035	**	AUC ((ΔF*t)/F)	SST
	W+CF	1.1582		0.0427			test				
2.I (c)	W	2.4758	2.269	0.107	177†	18	Wilcoxon	0.0032	**	AUC ((ΔF*t)/F)	PV
	W+CF	2.6768	2.369	0.1092							
2.I (r)	W	1	N/A	0	177	18†	One-sample t-	0.0127	*	AUC ((ΔF*t)/F)	PV
	W+CF	1.1122		0.0403			test				

† indicates whether statistics performed across cells or mice

panel		mean	median	error	n cells	N mice	test	*P* value	result	measurement (units)	cell type
3.C	Pre	5.2386	4.0088	0.8243	12	7	Wilcoxon	0.0425	*	AUC ((ΔF*t)/F)	SST
	DCZ	9.2671	5.9757	2.3962							
3.D (c)	Pre	5.7312	2.927	0.5212	255	4	Wilcoxon	<0.001	***	AUC ((ΔF*t)/F)	PN
	Post	3.106	1.9677	0.2207							
3.D (r)	Pre	0.3938	0.1934	0.0358	255	4	Wilcoxon	<0.001	***	Amplitude (ΔF/F)	PN
	Post	0.2139	0.1403	0.015							
3.G	Pre	8.9616	7.5298	1.1235	53	6	Wilcoxon	0.0057	**	AUC ((ΔF*t)/F)	SST
	DCZ	7.5387	6.4485	0.7883							
3.H (c)	Pre	7.8992	4.0365	1.0087	183	3	Wilcoxon	<0.001	***	AUC ((ΔF*t)/F)	PN
	Post	9.9871	4.5967	1.2894							
3.H (r)	Pre	0.5334	0.267	0.0682	183	3	Wilcoxon	<0.001	***	Amplitude (ΔF/F)	PN
	Post	0.6759	0.3062	0.0872							
4.C	Pre	1.1339	0.8779	0.3452	10	3	Paired t-test	0.0272	*	AUC ((ΔF*t)/F)	VIP
	DCZ	0.2521	0.2239	0.04							
4.D (c)	Pre	2.6299	1.8696	0.2739	189	3	Wilcoxon	<0.001	***	AUC ((ΔF*t)/F)	PN
	Post	1.4749	1.2773	0.0768							
4.D (r)	Pre	0.179	0.1242	0.02	189	3	Wilcoxon	<0.001	***	Amplitude (ΔF/F)	PN
	Post	0.1021	0.0849	0.0055							
4.G	Pre	1.3677	0.2754	0.8043	14	3	Wilcoxon	0.0494	*	AUC ((ΔF*t)/F)	VIP
	DCZ	1.9361	0.4533	1.0391							
4.H (c)	Pre	2.53	1.9726	0.1644	202	4	Wilcoxon	<0.001	***	AUC ((ΔF*t)/F)	PN
	Post	3.2011	2.2506	0.2818							
4.H (r)	Pre	0.1813	0.1324	0.0142	202	4	Wilcoxon	<0.001	***	Amplitude (ΔF/F)	PN
	Post	0.2309	0.1529	0.0226							

panel		mean	median	error	n cells	N mice	test	*P* value	result	measurement (units)	cell type
5.F	baseline	1.2386	N/A	0.11	5	5	Welch's t-test	<0.001	***	EPSP amplitude (mV)	ZI neuron
	+TTX	0.4094		0.081	3	3					
	baseline	3.4		0.4159	5	5	Welch's t-test	0.62	n.s.	Latency (ms)	
	+TTX	3.633		0.1333	3	3					
5.I	W (Baseline)	5.1648	3.2461	0.778	80	3	Wilcoxon	0.0183	*	AUC ((ΔF*t)/F)	PN
	W+CF (Baseline)	4.7113	3.1395	0.7239							
	W (DCZ)	3.6838	2.5494	0.6804			Wilcoxon	<0.001	***		
	W+CF (DCZ)	4.1972	2.7795	0.6946							

panel		mean	error	n cells	N mice	measurement (units)	cell type
S1.H (l)	3x15	0.3455	0.0198	102	1	Amplitude (ΔF/F)	PC
	2x20	0.3213	0.0177				
	1x50	0.554	0.023				
	(3x15)*2	0.3616	0.0171				
S1.H (r)	3x15	3.5376	0.2585	102	1	AUC ((ΔF*t)/F)	PC
	2x20	3.8521	0.2483				
	1x50	5.1302	0.3019				
	(3x15)*2	4.3732	0.261				

panel		mean	%	error	n cells	N mice	test	*P* value	result	measurement (units)	cell type
S2.C	Persistent (RWS)	N/A	86.793	N/A	318†	10	Chi-squared	0.0081	**	percent total cells (%)	PN
	Recruited (RWS)		7.2327								
	Suppressed (RWS)		4.4025								
	Unresponsive (RWS)		1.5723								
	Persistent (RWS+CF)		89.447		597†	11					
	Recruited (RWS+CF)		8.7102								
	Suppressed (RWS+CF)		1.5075								
	Unresponsive (RWS+CF)		0.335								
S2.D	Pre (RWS)	0.9427	0.4235	0.1916	318†	10	Wilcoxon	<0.001	***	AUC ((ΔF*t)/F	PN
	Post (RWS)	1.269	0.4767	0.196							
	Pre (RWS+CF)	1.1012	0.4755	0.1203	597†	11	Wilcoxon	0.9575	n.s.		
	Post (RWS+CF)	0.9152	0.5405	0.0697							
S2.E	-40 min (RWS)	1.31967	N/A	0.2614	226†	8	Two-way ANOVA	<0.001	***	AUC ((ΔF*t)/F	PN
	-30 min (RWS)	1.36211		0.2702	257†	9					
	-20 min (RWS)	0.54539		0.1912	281†	9					
	-10 min (RWS)	0.8977		0.1733	318†	10					
	0 min (RWS)‡	1.69982		0.4654	167†	6					
	10 min (RWS)‡	1.50865		0.2312	318†	10					
	20 min (RWS)‡	1.28199		0.2427	318†	10					
	30 min (RWS)‡	1.27499		0.3031	219†	8					
	40 min (RWS)‡	1.47304		0.2684	219†	8					
	50 min (RWS)‡	0.88172		0.1994	219†	8					
	60 min (RWS)‡	1.20839		0.3212	117†	4					
	- 40 min (RWS+CF)	1.42937		0.2614	583†	8					
	-30 min (RWS+CF)	1.15418		0.2702	597†	9					
	- 20 min (RWS+CF)	1.0151		0.1912	595†	9					
	-10 min (RWS+CF)	1.0404		0.1733	597†	10					
	0 min (RWS+CF)‡	0.93197		0.4654	565†	6					
	10 min (RWS+CF)‡	0.73911		0.2312	597†	10					
	20 min (RWS+CF)‡	0.99672		0.2427	597†	10					
	30 min (RWS+CF)‡	0.92438		0.3031	595†	8					
	40 min (RWS+CF)‡	0.80124		0.2684	595†	8					
	50 min (RWS+CF)‡	0.75768		0.1994	441†	8					
	60 min (RWS+CF)‡	1.05528		0.3212	422†	4					

† indicates whether statistics performed across cells or mice
‡ time points included in ANOVA

panel		mean	%	error	n cells	N mice	test	*P* value	result	measurement (units)	cell type
S2.F	Pre (RWS)	1.4169	0.7344	0.1201	590†	10	Wilcoxon	<0.001	***	AUC ((ΔF*t)/F	IN
	Post (RWS)	0.9556	0.4945	0.0861							
	Pre (RWS+CF)	1.4741	0.4905	0.1679	590†	11	Wilcoxon	<0.001	***		
	Post (RWS+CF)	1.5336	0.643	0.1391							
S2.G	-40 min (RWS)	1.72714	N/A	0.1726	455†	8	Two-way ANOVA	<0.001	***	AUC ((ΔF*t)/F	IN
	-30 min (RWS)	1.50359		0.1432	521†	9					
	-20 min (RWS)	1.2485		0.1425	484†	9					
	-10 min (RWS)	1.47982		0.1335	590†	10					
	0 min (RWS)‡	1.86324		0.211	353†	6					
	10 min (RWS)‡	1.14703		0.1116	590†	10					
	20 min (RWS)‡	0.96291		0.0994	590†	10					
	30 min (RWS)‡	1.0608		0.1103	408†	8					
	40 min (RWS)‡	1.28719		0.1177	408†	8					
	50 min (RWS)‡	0.64955		0.1004	408†	8					
	60 min (RWS)‡	1.19079		0.137	233†	4					
	- 40 min (RWS+CF)	1.55022		0.186	556†	10					
	-30 min (RWS+CF)	1.49275		0.1918	590†	11					
	- 20 min (RWS+CF)	1.54222		0.1819	574†	10					
	-10 min (RWS+CF)	1.37409		0.1664	590†	11					
	0 min (RWS+CF)‡	1.37262		0.1791	506†	10					
	10 min (RWS+CF)‡	1.46844		0.1439	590†	11					
	20 min (RWS+CF)‡	1.615		0.1589	590†	11					
	30 min (RWS+CF)‡	1.37859		0.1462	574†	10					
	40 min (RWS+CF)‡	1.15724		0.1187	574†	10					
	50 min (RWS+CF)‡	1.71047		0.1918	356†	6					
	60 min (RWS+CF)‡	2.15427		0.1933	309†	4					
S2.H	Pre (RWS)	0.7676	0.408	0.0852	106†	8	Wilcoxon	0.0161	*	AUC ((ΔF*t)/F	PV/SST
	Post (RWS)	0.6342	0.4891	0.0734							
	Pre (RWS+CF)	0.66	0.3357	0.0895	144†	7	Wilcoxon	0.4728	n.s.		
	Post (RWS+CF)	0.626	0.4079	0.0634							
S2.I	-40 min (RWS)	1.08381	N/A	0.1371	60†	5	Two-way ANOVA	0.2226	n.s.	AUC ((ΔF*t)/F	PV/SST
	-30 min (RWS)	0.72739		0.095	95†	6					
	-20 min (RWS)	0.53799		0.1191	85†	6					
	-10 min (RWS)	0.82889		0.1025	106†	7					
	0 min (RWS)‡	1.08367		0.1267	65†	4					
	10 min (RWS)‡	0.84968		0.0955	106†	7					
	20 min (RWS)‡	0.6124		0.0826	106†	7					
	30 min (RWS)‡	0.59868		0.1062	71†	6					
	40 min (RWS)‡	0.81768		0.1347	71†	6					
	50 min (RWS)‡	0.4411		0.0992	71†	6					
	60 min (RWS)‡	0.65544		0.138	37†	3					
	- 40 min (RWS+CF)	0.82654		0.1226	144†	8					
	-30 min (RWS+CF)	0.7202		0.1322	144†	8					
	- 20 min (RWS+CF)	0.67888		0.0845	144†	8					
	-10 min (RWS+CF)	0.60953		0.0921	144†	8					
	0 min (RWS+CF)‡	0.56119		0.116	107†	7					
	10 min (RWS+CF)‡	0.61031		0.0631	144†	8					
	20 min (RWS+CF)‡	0.60364		0.071	144†	8					
	30 min (RWS+CF)‡	0.5373		0.0795	144†	8					
	40 min (RWS+CF)‡	0.64281		0.0654	144†	8					
	50 min (RWS+CF)‡	0.63526		0.081	76†	4					
	60 min (RWS+CF)‡	1.0077		0.1262	76†	4					

† indicates whether statistics performed across cells or mice

‡ time points included in ANOVA

panel		mean	median	error	n cells	N mice	test	*P* value	result	measurement (units)	cell type
S3.B	PN	0.0072	-0.0021	0.0023	1136	24	N/A	N/A	N/A	xCorr (r)	PN
	IN	0.032	0.0114	0.0023	1594	34				xCorr (r)	IN
	PV	-1.47E-04	-2.72E-04	0.0046	221	13				xCorr (r)	PV
	SST	0.0346	0.0312	0.0114	73	6				xCorr (r)	SST
	VIP	0.0899	0.0788	0.0082	164	8				xCorr (r)	VIP
S3.D (top l)	Rest	35.21	N/A	11.67	N/A	10†	Chi-squared	0.0079	**	percent total trials (%)	N/A
	Active	64.14		11.52							
	Stop	0.66		0.356							
S3.D (bottom l)	Rest	28.96		11.52							
	Active	70.61		11.58							
	Stop	0.43		0.2881							
S3.D (top r)	Rest	33.46		13.36		11†	Chi-squared	<0.001	***		
	Active	66.54		13.36							
	Stop	0		0							
S3.D (bottom r)	Rest	42.4466		14.3875							
	Active	57.3183		14.4512							
	Stop	0.2351		0.1579							
S3.H	Pre (RWS)	4.0059	2.1655	0.7509	124†	10	Wilcoxon	0.0147	*	AUC ((ΔF*t)/F)	PN
	Post (RWS)	5.7207	2.2396	1.5931							
	Pre (RWS+CF)	2.677	1.7382	0.1927	388†	11	Wilcoxon	0.5104	n.s.		
	Post (RWS+CF)	2.4344	1.7958	0.1195							
S3.I	Pre (RWS)	3.3914	2.3096	0.2246	212†	10	Wilcoxon	0.0033	**	AUC ((ΔF*t)/F)	IN
	Post (RWS)	2.965	2.0138	0.2076							
	Pre (RWS+CF)	3.3041	2.2275	0.2025	296†	11	Wilcoxon	<0.001	***		
	Post (RWS+CF)	3.5204	2.2994	0.1901							

† indicates whether statistics performed across cells or mice

panel		mean	error	N mice	test	*P* value	result	measurement (units)
S4.C	RWS (Pre) RWS (Post)	1 3.6978	0 0.8273	4	one-sample t-test	0.0471	*	Whisker responsive area
	RWS+CF (Pre) RWS+CF (Post)	1 0.5195	0 0.2171	4		0.1138	n.s.	
	control (Pre) control (Post)	1 1.5067	0 0.1176	4		0.0649	n.s.	

panel		mean	median	error	n cells	N mice	test	*P* value	result	measurement (units)
S5.B	Pre	2.8467	2.507	0.1745	220†	3	Pre vs DCZ: Wilcoxon DCZ vs Post: Wilcoxon	Pre vs DCZ: <0.001 DCZ vs Post: <0.001	Pre vs DCZ: *** DCZ vs Post: ***	AUC ((ΔF*t)/F)
	DCZ	1.587	1.2817	0.0809	218†					
	Post	1.7015	1.4958	0.0726	220†					
S5.C	Control	0	0.0212	0.0631	218†	3	Wilcoxon	<0.001	***	Corrected ΔAUC
	Plasticity	-0.14	-0.2199	0.0509	253†	4				
S5.E	Pre	4.2185	3.0214	0.3601	181†	3	Pre vs DCZ: Wilcoxon DCZ vs Post: Wilcoxon	Pre vs DCZ: <0.001 DCZ vs Post: 0.0422	Pre vs DCZ: *** DCZ vs Post: *	AUC ((ΔF*t)/F)
	DCZ	2.9159	2.2613	0.2104	177†					
	Post	2.5923	2.1445	0.1419	177†					
S5.F	Control	0	-0.0686	0.0655	173†	3	Wilcoxon	0.6742	n.s.	Corrected ΔAUC
	Plasticity	-2.469	-0.0227	2.9139	164†	3				
S5.H	Pre	4.3825	2.7846	0.425	181†	3	Pre vs DCZ: Wilcoxon DCZ vs Post: Wilcoxon	Pre vs DCZ: 0.0018 DCZ vs Post: <0.001	Pre vs DCZ: ** DCZ vs Post: ***	AUC ((ΔF*t)/F)
	DCZ	4.3789	3.374	0.3058	185†					
	Post	3.8364	2.8455	0.2325	180†					
S5.I	Control	0	-0.2341	0.0623	175†	3	Wilcoxon	0.0928	n.s.	Corrected ΔAUC
	Plasticity	0.1359	0.0253	0.0409	181†	3				
S5.K	Pre	2.4242	1.9103	0.2445	136†	3	Pre vs DCZ: Wilcoxon DCZ vs Post: Wilcoxon	Pre vs DCZ: <0.001 DCZ vs Post:0.0902	Pre vs DCZ: *** DCZ vs Post: n.s.	AUC ((ΔF*t)/F)
	DCZ	3.1922	2.6613	0.2031	137†					
	Post	3.0724	2.5155	0.2135	137†					
S5.L	Control	0	0.0021	0.022	145†	3	Wilcoxon	<0.001	***	Corrected ΔAUC
	Plasticity	0.1723	0.0982	0.0351	197†	4				

† indicates whether statistics performed across cells or mice